A study on local neuro mass dynamics in the neocortex of rats

Doctoral Thesis

A study on local neuro mass dynamics in the neocortex of rats

ラット大脳新皮質における局所神経細胞群動特性の解明

Takeshi Ogawa

Department of Functional Brain Imaging,

Tohoku University Graduate School of Medicine

ABSTRACT

"A study on local neuro mass dynamics in the neocortex of rats"

submitted by

Takeshi Ogawa

Advisors: Prof. Jorge Riera and Prof. Ryuta Kawashima

It has been pointed out recently that sound codification in the primary auditory cortex (A1) of rats is accomplished through neuronal networks with functional distributions by layer. Sparsely organized pyramidal cells (PCs) reside in the supragranular layer (SG layer) while dense-distributed PCs reside in the infragranular layer (IG layer). PCs from both populations, together with putative interneurons (INs), do not always show trivial tuning characteristics for fundamental sound attributes, as it was thought in the past. However, the spatial localization of such specialized neuronal networks has not been investigated. Furthermore, most of these neurons have been classified from the signatures they leave on multiunit activity (MUA), but the relationships that neuronal spiking has with underlying sub/supra-threshold postsynaptic activities (i.e. local field potential: LFP) have not yet been clarified.

In this thesis, therefore, we aim to clarify the sound codification system in A1 on the mesoscopic scale. To this end, we examined the following topics: **a)** the spatial aggregation to codify sounds attributes in A1; **b)** the spike-LFP relationships for the codifying neuronal

population in layers II/III, IV, and V; **c)** the laminar profiles for the different neuron types of those populations that employ dissimilar schemes for attribute codification in the A1 of Wistar rats.

We used extracellular potentials recorded simultaneously from 64 sites inside the A1 of adult Wistar rats, based on the MRI guide's method. These extracellular potentials were used to evaluate neuronal codifiers for fundamental attributes, which were selected for their peculiar MUA dose-response curves. Second, we estimated the current source density (CSD) and the time-variant power spectrogram from LFPs in each layer. After that, we evaluated the temporal correlation between MUA and CSD.

We demonstrated that the neuronal populations lying behind MUA and CSD were sparsely and heterogeneously distributed along the A1, even though the compilation of them showed tonotopic organization. The majority of codifying neurons were PCs showing laminar profiles. MUA was correlated to β postsynaptic oscillations in the IG layer, while the SG layer revealed a better correlation between MUA and γ_H postsynaptic oscillations.

We concluded that, for rats, sounds are codified in the A1 by a sparsely segregated network involving specialized PCs. Additionally, their postsynaptic activity may create the proper conditions for the emergence of sparse and dense spiking patterns.

Contents

Chapter 1. Introduction

1.1 Topological sounds representation in the neocortex

1.1.1 Tonotopic representation

The codification of the fundamental attributes of a sound, i.e. the timbre, the pitch, and the loudness, has for many years now been thought to occur by means of topologically distributed assemblies of neurons exhibiting attribute-dependent tuning effects, which exist at several auditory relay regions along the afferent pathway. The *tonotopic representation* constitutes the most universal of such topological distributions for sound segregation in mammals, i.e. a correlation between spatial locations and preferable pure tone frequencies which is preserved from the cochlea to the neocortex[1) - 4)]. Frequency selective neurons usually show V-shape tuning curves with spectral bandwidth Q_{10} (Q_{40}) for the near (away) response threshold. In the primary auditory cortex (A1), such organization was discovered in cats by Woosley and Walzl[5)]. The tonotopic representation has not only been described initially by electrophysiological recordings based on multi-unit activity (MUA)[6)], but lately, also by more contemporaneous recording techniques such as the optical imaging of intrinsic signals[7), 8)].

1.1.2 Iso-frequency axis

A consensus has not yet been reached on whether or not a spatial code for the periodicity of sounds in the A1 of mammalians exists. Although some studies have reported that a pitch-selective area in monkeys likely exists along the borderline delimiting the rostral field and A1[9), 10)], others have proposed that neurons sensitive to pitch variations spanned the entire A1 for both rats[11)] and ferrets[12), 13)]. These pitch-selective neurons have a peculiar spatial organization along the dorso-ventral axis of A1, as revealed using optical intrinsic signals in cats[14)]. The role of the neurons, which is to select a sound's particular pitch, has been explored recently[15), 16)]. Our understanding of the spatial organization of neurons sensitive to the amplitude of sounds is rather incomplete. An early work by Schreiner et al. (1992), who based the analysis of topological codifiers on five parameters (i.e. threshold, transition-point, SRL, dynamic-range and monotonicity), was a major contribution[17)]. These parameters originated from the dose–response curves for the spiking rate of particular neurons in the A1 of cats. Robust changes in the amplitude thresholds for characteristic frequencies have been found along the iso-frequency curves[18)]. Nonmonotonic level coding schemes in the A1, known as intensity tuning, have been proposed to account for the level-invariant representations of the spectrum coding[19), 20)] and the specialized coders of low sound levels[21)].

1.2 Laminar structure in the primary auditory cortex

1.2.1 Anatomical structure of the primary auditory cortex

In order to delineate and integrate auditory information, the sequence of processing and the flow of information are governed by stereotypical and precise connections between cortical layers. The auditory information from the thalamus enters the cortex by way of thalamocortical synapses. From the thalamocortical synapses, the information enters the neurons in cortical layer IV and these layer IV neurons then transmit information to neurons in layer II/III. Finally, information is transmitted to layer V[22), 23)]. The morphometory of neurons in layer II and layer III pyramidal cells are different: layer III neurons had a classic pyramidal shape, whereas layer II cells lacked an elongated apical shaft and instead had dendrites that arborized parallel to the slice. At the level of local connectivity, the pattern of intracortical synaptic input was also distinct between these layers, especially along the tonotopic axis: layer II received columnar input, whereas layer III received out-of-column input. Some of the neurons in layer III projected to the contralateral cortex, as observed in the auditory cortex of the cat and rat[24)].

In the somatosensory and visual cortices, layer IV can be identified by the presence of a dense band of granule cells containing a high proportion of spiny interneurons[25)]. Consequently, it is relatively easy to define the borders of layer IV. However, the auditory cortex has comparatively few spiny interneurons in layer IV and the faint “granular”

appearance it retains is due to the high proportion of small pyramidal neurons that are also present in layer III and V[26]. The lack of the dense aggregation of granule cells that define layer IV in layer III and V makes it difficult to identify either border of layer IV. Layer III and IV of the A1 merge into each other in both layers. The excitatory interneurons seem to be evenly distributed across all cortical layers of the A1 and may be associated with a different form of intrinsic processing than the other primary sensory areas[18].

1.2.2 Functional laminar profile in the primary auditory cortex

In recent studies, the layers create a difference in how auditory information is processed. We would like to highlight two studies very relevant to the results reported in the present study: i) the existence of layer-dependent processing modes[15] and ii) the sparse organization of the neuronal codifiers in layers II/III[27]. Sakata and Harris (2009) found that the propagation patterns of neuronal activity in the layer II/III is sparse, but the neurons in layer V are densely activated[15]. Rothschild et al. (2010) observed neuronal processing at the cellular level by using an *in vivo* Ca^{2+} imaging technique in layers II/III A1 of mice. They found that neurons with the same preferential stimulus condition were not clearly organized, but they were connected to each other internally [27].

1.3 Neuronal processing on the mesoscopic scale

1.3.1 Electrophysiological recording on the mesoscopic scale

In the last two decades, biomedical engineers developed miniaturized silicon-based electrophysiological probes (multi-electrode array: MEA) which are composed of different spatial arrangements of shanks and a variety of microelectrode local configurations (Figure 1.1)[28]. Using MEAs we can observe the extracellular potentials in all layers with high spatial resolution. From the recorded potentials, we can obtain low- and high-frequency signals called local field potentials (LFPs) and multi-unit activity (MUA), respectively. The postsynaptic activity creates gradients of potentials within the cortex which could be equivalent to the primary current source density (PCD). The method used to estimate PCD from LFPs is the current source density (CSD) analysis. PCD is equivalent to the CSD. Synchronized neuronal activities can be observed as MUA. Thus, extracellular recording on the mesoscopic scale is important for exploring the relationship between LFPs and MUA, and between LFPs and the electroencephalogram (EEG). Additionally, in order to interpret the physiological mechanism from those datasets, a proper analysis based on a physiological assumption is required. Mesoscopic scale recording involves three essential topics (a) spike sorting methods (b) identification of neuron-types, and (c) characterization of synaptic inputs[28) - 30)].

1.3.2 Local field potentials

Local field potential (LFP), the low-frequency part of the extracellularly recorded potential, is generated by the transmembrane currents of neurons. The potential is made of external reflections which come through a conductive extracellular medium of the ionic currents flowing across excitable membranes. The study of LFP is useful for understanding the genesis and propagation of long-lasting, time integrative, and the postsynaptic potentials ranging from several hundred micrometers to a few millimeters on the mesoscopic scale[28), 31)]. The oscillations of the extracellular potentials are observable anywhere in the extracellular medium.

LFP contains neuronal oscillations which are rhythmic alternations such as δ (1−4 Hz), θ (4−8 Hz), α (8−12 Hz), β (12−30 Hz), γ-low (30−90 Hz), and γ-high (90−170 Hz) waves. We summarized the role of each frequency band of LFP in Table 1.1. These oscillations play a role in various types of information processing in the brain, e.g. sleep, neuronal interactions between brain areas[32), 33)], memory formation[34)], and cognitive control of sensory input[35)]. The time series of the above types of neuronal activities can be generally assessed by means of statistics computed in the time-frequency domain. The most common approaches are the use of a short-term Fourier transform (sFFT), Hilbert transform[35)], Gabor[36)] or wavelet transform[32), 33),37)], all of which are equivalent representations of the time series in terms of complex coefficients at each time and frequency (Figure 1.2). The power

and phase of a particular frequency band is obtained from the norm and angle of the complex coefficients, respectively.

The coupling of the neuronal frequency band could estimate neuronal activity (e.g. the MUA) in the sensory stimulus condition. The amplitude and phase of the low frequency band (δ or θ) and high frequency band (γ) are correlated, which is called *phase-amplitude coupling* (PAC) or *frequency band coupling* (FBC). These couplings could be credible estimators of the MUA under a visual attention task or multi-sensory evoked condition in monkeys. α and β oscillations are observable in the cortex for the neuronal activity of non-stimulus conditions such as sleep[38] or an anesthetization [39]. These oscillations are called *spindle* and their signal is a strongly non-stationary process. Spindle, observed in the primary sensory cortex, is generated by interneuronal oscillations in the thalamus. It propagates to the cortex along the thalamo-cortical pathway.

In sum, LFP is largely observable and allows the information process to be accessed from the mesoscopic scale to the macroscopic scale.

1.3.3 Current source density analysis

A CSD analysis is required for obtaining a good estimation of the underlying brain sources from LFPs. CSD analyses serve to illustrate instantaneous spatial profiles of local transmembrane currents, especially excitatory synaptic activations. LFPs are also thought to

be one genesis of EEG signals based on the dendritic processing of synaptic input. However, a direct interpretation from the physiological point of view is difficult. In certain cases, the CSD analysis is useful because it is a general method for the estimation of the CSDs from the measured LFPs. LFPs allow situations such as i) spatially confined cortical activity and ii) spatially varying extracellular conductivity to be handled. In recording with the MEA, the data set of LFPs consists of temporal and spatial information. Temporal information contains multiple frequency-band oscillations, which are time-variant non-stationary signals. In this case, the time-frequency analysis is carried out by means of some form of time-localized Fourier decomposition of single trials. In contrast, spatial information, such as the position of the electrode and the potentials, provides the position of excitatory synaptic activity. The CSD analysis provides us with the location of the current source and the spatial morphometry of the PCs in the cortex[40) - 43)].

1.3.4 Multi-unit activity

Neuronal communication, which includes transformation, transmission and storage of information in the brain, is based mainly on the action potentials of the neuronal population. Action potentials produce large transmembrane potentials in proximity to their somata. These output signals propagate through a conductive medium into the extracellular space and can be measured by voltage with an insulated wire or electrode. A distance of 20 μm from the tip of

the electrode to the cell body can identify a given neuron's extracellularly recorded spikes. However, in a single unit recording it is difficult to find which neuron is activated by the behavior or sensory stimulus. In contrast, the MEA can observe a hundred to a thousand neurons simultaneously in the extracellular space[28]. A method to analyze the multiple recorded neurons is required to identify and classify neuronal populations. Therefore, the methods used to identify neurons are important for understanding what the extracellular action potential is and what its features are.

1.3.5 Spike sorting

Spike sorting is a method to detect spikes and identify neuronal populations. The procedures of spike sorting are basically as follows: **a)** detecting spikes from extracellular recorded data, **b)** extracting the character of multiple spike shapes, and **c)** classifying the spike patterns of neurons based on the extracted features. There are several basic methods for detecting the multiple spike shapes: the principle component analysis (PCA)[30), 44) - 46)], the independent component analysis (ICA)[47)], and the wavelets method[48)].

For spike sorting, the recorded data in the extracellular space is filtered with a high-frequency band (500–5000 Hz). Then several action potentials are detected with a threshold of 3−5 SD of the signals, in general. A simple way to classify the neuronal population is to measure features of the spike shape, such as spike height and width or

peak-to-peak amplitude. Plotting all of the spikes are as points and identifying the characteristics of the neurons to which a cluster belongs is one of the earliest approaches to spike sorting.

The clustering method is a technique to reveal clusters that are relevant to the classification of spike shapes. However, it is difficult to detect cluster boundaries without the aid of a computer. The analysis finds clusters in multi-dimensional data sets and classifies the data based on those clusters. A basic assumption underlying the clustering methods is that the data is the result of several independent classes, each of which can be described by a relatively simple model. This assumption fits the case of spike sorting rather well, as each action potential arises from different neurons[49]. The first task of clustering is to describe both the cluster location and the variability of the data around that location. The second task is, given a description of the clusters, to classify new data. A simple approach to classifying the data is the nearest-neighbor, or *k-means*, clustering which defines cluster locations as the mean of the data within that cluster[50]. A spike is classified to whichever cluster has the closest mean to it using the Euclidean distance. This method of classification defines a set of implicit decision boundaries that separate the clusters. Other approaches are the Bayesian classification[49] and superparamagnetic clustering[48], from which it is possible to obtain some idea of how well separated a class is from others.

Chapter 2. The purpose of thesis

Previous electrophysiological studies of A1 have mainly investigated the neuronal response to certain auditory stimulations or a particular neuronal response feature for several auditory stimulation paradigms in a particular layer. These observations in A1 could be focused on local neuronal activity, rather than neuronal population activity on the mesoscopic scale; except in a few studies[15), 33)]. In order to interpret the underlying mechanism of the neuronal population's activities on the mesoscopic scale in A1, however, we need to explore how neuronal population activity is recorded and which analysis should be applied. To this end, it is important to understand the relationship between LFPs and MUA. Furthermore, due to the expansion of the observable space, the feature extraction method is required to understand the large and complex recorded dataset.

In this thesis, our aim is to clarify the sound codification system in A1 on the mesoscopic scale. Thus, we will examine these main questions: **a)** the spatial aggregation to codify sounds attributes in A1; **b)** the spike-LFP relationships for codifying neuronal population in layers II/III, IV, and V; **c)** the laminar profiles for different neuron types of those populations that employ dissimilar schemes for attribute codification in the A1 of Wistar rats.

Chapter 3. Material and Methods

All experiments in the measurements were performed in agreement with the policies established by the "*Animal Care Committee*" at Tohoku University, Sendai, Japan. In this thesis, we performed three new techniques: **a)** we co-registered a rat brain atlas to localize A1 for the a probe insertion; **b)** we performed a 3D extracellular recording in the A1 of rats under the complex audio stimulation in order to elucidate the relationship between LFPs and MUA in the sound processing; **c)** we calculated instantaneous CSD for each layer and obtained correlations between them and the instantaneous MUA.

3.1 A hand-made combination three-dimensional probe

Our hand-made combination three-dimensional probe (3D probe) consists of two planar acute silicon-based probes (*a4×8-5mm100-400-177*, Neuronexus Technologies, Ann Arbor, MI) tightly attached with superglue. Each planar probe comprises 32-channels (8 active sites on 4 parallel probes with a vertical spacing of 100 μm). These two probes were assembled by hand with the help of the S6D microscope (LEICA, Wetzlar, Germany) in such a way that the shanks of both probes are parallel and their tips are aligned[51]. The distance between the planar probes for all experiments was 450 ± 50 μm. We evaluated the accuracy of the 3D probe

insertion in A1 from information in the vessel distribution. For each experiment, the relative position of the 3D probe and the vessels was obtained from both high-resolution photographs of the craniotomy area and the DiI-based vessel staining (Figure 3.1 B). The 3D probe was successfully inserted into A1 in three rats and partially inserted in the other four. In the analysis performed henceforward, we employed only those shanks that were allocated inside A1.

3.2 MRI anatomical imaging and co-registration to the rat atlas

Animal experiments were performed in male Wistar rats (287−386g, N = 12). MRI data were acquired using a 7 Tesla Bruker PharmaScan system (Bruker Biospin, Ettlingen, Germany) with a 38-mm-diameter birdcage coil. Each rat was initially anesthetized with 5% isoflurane and then secured on a custom-built holder using adhesive tape and a bite bar. A breathing sensor (SA Instruments Inc., NY) was placed under the ventral face of the rat body. Anesthesia was further maintained with isoflurane (at 1 *l*/min oxygenation), administered via a face mask. Constant breathing rate was maintained around 50 breaths/min during MRI acquisition by manually maintaining the concentration of isoflurane at 1.5−2.5 %. Core body temperature was maintained at 37.0 ± 1 °C by means of a hot water-circulating pad. High

resolution T2-weighted images were obtained using a respiratory-gated 2-D TurboRARE sequence with fat suppression under the following parameters: TR = 4628 ms, TEeff = 30 ms, RARE factor = 4, effective spectral bandwidth = 100 kHz, flip angle = 90 degree, field of view = 32 × 32 mm^2, matrix size = 256 × 256, in-plane resolution = 125 × 125 μm^2, number of slices = 54, slice thickness = 0.5 mm, slice gap = 0 mm, and number of averages = 10. The total scanning time for T2-weighted imaging was about 50 min, depending on the respiration rate for each rat. T2-weighted images were utilized for normalization to the template of the rat brain atlas (Valdés-Hernández et al., under revision), which was, by construction, co-registered to a digitalized-atlas[52]. The normalized T2-weighted images were converted back to the native space (Figure 3.1 A, left: axial slice, center: coronal slice). The actual positions of two crucial landmarks for stereotaxic-guided craniotomy in rats, i.e. the bregma and the lambda, were also determined from the individual T2-weighted images. In the same way, we calculated approximately the point (P_{A1}) where the A1's center projects perpendicularly to the antero-posterior axis defined by these landmarks, a step that allowed us to determine the lateral distance from the sagittal suture to the center of the surface of A1. Based on the MRI data, we planned the site for the craniotomy as illustrated in Figure 3.1 A (right).

3.3 Surgical procedures

In the electrophysiological experiments, anesthesia was induced with urethane (1.2 g/kg). The animal was placed on a stereotaxic stage, and the temporal muscles on the right side were retracted. A craniotomy was performed over the A1 based on the MRI-guidance and the accuracy of the method was latterly confirmed by the vessel distribution (Figure 3.1 B, top right). The dura was removed under the digital microscope KH-1300 (HIROX, Tokyo, Japan), and the cortex was covered with HEPES-buffered and Ca^{2+}-free aCSF (150 mM NaCl, 2.5 mM KCl, 1 mM $MgCl_2 \cdot 6H_2O$, 10 mM HEPES, 10 mM glucose, the pH was adjusted to 7.4 with tris-base). Two screws, used as a reference and ground for the extracellular recordings, were attached to the skull close to the lambda on the cerebellum[53].

3.4 Electrophysiological recording

The insertion length and angle of the 3D probe were accurately monitored/corroborated through a micromanipulator's control system (SM5, Luigs & Neumann, Ratingen, Germany). The 3D probe was perpendicularly inserted 1050 μm into the cerebral cortex, the observable depth was 300−1000 μm from the surface. The microelectrode impedance in the probe ranged from 0.7−0.9 MΩ.

Extracellular potentials were recorded using amplifiers at 25 kHz (PZ2, TDT, Alachua,

FL) connected by an optical fiber to a signal processing unit comprising eight parallel CPUs (RZ2, TDT) and by a coaxial cable to a preamplifier located inside two acute 32-channel 18-bit hybrid headstages, respectively. By means of the 3D probe, we were able to simultaneously record extracellular potentials from eight different sites along the A1's surface, a total of 64 channels (Figure 3.1 B, bottom). All recordings were performed using an online logic/symbolic programming language supported by signal processing unit (OpenEx software, TDT).

3.5 Auditory stimulation protocol

The auditory stimulation system was described in Figure 3.2 A. Acoustic stimuli were generated digitally by a custom-written code in MATLAB (R2009b, The Math Works, Natick, MA) and delivered with a D/A converter (National instruments, Austin, TX) and a speaker driver ED1 (TDT) to a calibrated condenser speaker ES1 (TDT). The stimuli were presented to the anesthetized animals, which were placed in a single-walled soundproof box, though a speaker with a customized ear tube inserted into the left ear canal (VIC international, Tokyo, Japan). Speaker calibration was conducted with a condenser microphone (UC-29, RION, Tokyo Japan) close to the tip of the ear tube. Before performing the amplitude modulation sound stimulation, we performed a pure tone stimulation paradigm (N = 5; 100 ms long;

carrier frequency: 8 kHz steps, 8−40 kHz; peak of amplitude: 10 dBSPL steps, 30−70 dBSPL, inter-stimulus-interval: 900 ms, repetition: 20 trials). The amplitude modulation sound (N = 6; 200 ms long; carrier frequency: 16 kHz steps, 8−40 kHz; modulator frequency: 50, 200 and 800 Hz; peak of amplitude: 20 dBSPL steps, 30−70 dBSPL, inter-stimulus-interval: 1.6 s, repetition: 10 trials, Figure 3.2 B) was the acoustic stimuli [14]. Twenty-seven conditions were randomly prepared from the three sound attributes, i.e. frequency (f_c), amplitude (Amp), and modulation (f_m). One block contained all conditions and stimulation was repeated 10 times (Figure 3.2 B, bottom). 100-trial evoked potentials in total were recorded in each condition.

3.6 Immunostaining

In order to co-localized the shanks of the 3D probe, DiO (Invitrogen) was gently applied to the surface of the back-side of the shank before insertion. After the electrophysiological experiments, each rat was transcardially perfused with 10 ml PBS, 10 ml PBS with 200 µl DiI (Invitrogen) for vessel staining and then fixed with 10 ml 4% paraformaldehyde[54]. Finally, the brain was removed and post-fixed in the same fixative all night at 4°C. A fluorescent image (Figure 3.1 B, top-left) containing information 2 about the shank positions (yellow-green) and the vessel distribution (bright red) was captured with an upright fluorescent microscope (SZX16). A sketch with the distribution of principal vessels

was produced for each rat (Figure 3.1 B, top right). Coronal sections (100- μm thickness) from the entire A1 were obtained from the post-fixed brains with Vibratome 1000-plus (LEICA). Fluorescent Nissl staining of each brain section was additionally performed[51]. Nissl staining images, co-localized with the shank traces, were obtained with the SZX16 microscope (Figure 3.1 C).

3.7 Data processing

3.7.1 Pre-processing of the electrophysiological data

In Figure 3.3, we illustrated the flow chart of data processing. The extracellular potentials were processed by a custom-written code in MATLAB. LFPs and MUA were separated by the low-frequency bandpass filter (1−170 Hz, Figure 3.3, left part) and the high-frequency bandpass filter (500−5000 Hz, Figure 3.3, right part) respectively. The design of the bandpass filters was the Butterworth IIR-type. Single trial auditory-evoked potentials (**AEPs**) were estimated from the LFPs using the stimulus triggers, which were also recorded by an extra analog channel.

3.7.2 MUA analysis: Codifiers of sound attributes

Spike sorting was performed offline. We used a free-downloaded toolbox, "wave clus", for semi-automatic detection of spike time [48]. An amplitude threshold of 3.5 SD of the mean

amplitude was used for spike detection in each channel. A spike occurring within 1.5ms of the previous spike was not recognized[35]. The window size to count spiking rate was 10 ms and it moved in 1 ms- steps. In order to identify possible cortical sites for attribute codifiers, first the MUA in the eight channels of the same shank were normalized and integrated (Figure 3.4 A, example: 8 kHz, 50 Hz, 70 dBSPL). A respective interpolated-topographic map was created from the instantaneous (normalized/integrated) MUA in all shanks (Figure 3.4 B, 15 ms after onset). A peri-stimulus time histogram (PSTH) was calculated from the integrated MUA and compared with different conditions to define a particular codifier (Figure 3.4 C, shank 8 may contain information about a neuronal population codifying the amplitude of the tone with a carrier frequency of 8 kHz modulated at 50 Hz).

3.7.3 Time frequency analysis for LFP in three layers

In order to evaluate the relationship between LFP and the three layers in the frequency domain, the spectrograms of pre- and post stimulus (from - 50 ms to 250 ms) were computed by sFFT for each trial. Normally, the power spectrum contains a low frequency component; hence, it is hard to identify the high frequency time-variant power (1/f problem). One of the ways to solve the 1/f problem is the Z score transformation. After calculating the mean spectrogram of all trials, the mean and the standard deviation of all frequency power in the pre-stimulus states were estimated following as: $P_{Z\_All} = (P_{All} - \text{mean}(P_{pre})) / \text{std}(P_{pre})$,

where, P_{Z_All} is Z score matrix (time by frequency), P_{All} is the power spectrum, P_{pre} is the power of pre-stimulus.

3.7.4 CSD analysis and amplitude-phase analysis

We used the iCSD method[43] for a single shank with 8 channels (Appendix I). Therefore, the parameters used in this analysis were: **a)** 0.5 mm for the disk diameter d of the sources, **b)** 50 μm for the standard deviation of the Gaussian filter, and **c)** 3 mS/cm for the electric conductivity (homogenous media)[51]. The thickness l of the cortical columns for the A1 cortex was 2 mm. Assuming the barrel columns are perfect cylinders, their volumes $V = \pi (d/2)^2 l$ would be 0.39 mm^3. The CSD maps, resulting from the single trial AEP, were divided into three time-series, which summarized the CSD amplitude in the supra-granular (SG: 250−450 μm), granular (G: 450−650 μm), and infra-granular (IG: 650−950 μm) layers (Figure 3.5 A). Each time series was filtered (bi-directional bandpass filter) using six frequency bands (δ, θ, α, β, γ_L, γ_H). The Hilbert transfor was applied to each final filtered time series to extract instantaneous amplitude and phase for each single trial (Figure 3.5 B)[35].

3.7.5 Laminar profile of MUA and classification of neuron types

In order to classify the neuronal population associated with each codifier, the extracted spike-waveforms of single channels were clustered by the super paramagnetic

clustering method (**SPC**)[48]. The mean waveforms of all clusters were obtained from all channels, and used to calculate the peak amplitude asymmetry, half width, and trough peak[60]. Peak amplitude asymmetry is (b - a) / (b + a), where, a is the pre-positive peak of the mean-spike waveform, b is the post-positive peak of the mean-spike waveform. These three parameters were projected in the 3D space and used to classify wide-spiking cells (putative pyramidal cells: **PCs**) and narrow-spiking cells (putative interneurons: **INs**) (Figure 3.6 AB). From this classification of PCs and INs, we calculated the laminar profile of a raster plot and a peri-stimulus time histogram (PSTH, Figure 3.6 C).

3.7.6 Classification of codifier

An unmanageable number of neurons with differentiated functionality in the A1 may additionally be distributed in space. Neurons that might play an important role in codifying auditory signals have been identified from their particular responses (i.e. the spike rate) to variations in sound parameters. The most established auditory codifier is associated with neurons that show tuning characteristics[8), 11), 15)], in particular either frequency bands or sound levels. We discriminated such kinds of neurons by building up their intensity-frequency response maps.

Sounds are represented by a small fraction of neurons instead of being encoded by large numbers of neurons (i.e. a dense representation). Therefore, we decided to lose

specificity in the classification of neurons, to some extent, in order to achieve an appropriated identification of the spatial characteristics of those neurons showing reactivity to variations in sound attributes. In what follows, we describe our strategy to classify neurons that, in our opinion, are engaged in sound codification.

As described in the materials and methods, the spiking rates of all electrodes (eight) on a single shank were normalized and integrated 15 ms after the stimulus onset. From these summarized values of the laminar MUA in every experiment, we constructed square boxes for each shank by varying pairs of sound attributes (Table 3.1). We explored all shanks that were sensitive to changes in a particular sound attribute. Figure 3.7 A shows an example of the codifying profile for the sound amplitude (*Amp*) from the f_m-Amp box, as observed by shank-8 at three values of the carrier frequency. Rows in this box summarize the normalized MUA at different sound amplitudes (i.e. 30 dB, 50 dB, 70 dB) for particular modulation frequencies f_m. We chose this particular example because it contains the four types of codifiers (red curves) we were looking for: *positive slope*, *negative slope*, *U-shape*, and *inverted U-shape*. We applied the same criterion from the Amp-f_c and f_c- f_m boxes to classify codifiers.

A codifier revealing a normalized MUA that decreased or increased with the attribute value was called a "*negative slope*" or "*positive slope*" codifier, respectively. In contrast, a codifier having a maximum or a minimum middle value of the normalized MUA of the

attribute was called an "*inverted U-shape*" or "*U-shape*", respectively. We determined the manifestation of a codifier by the maximum-minimum difference. In the four types of codifiers mentioned above, if the maximum-minimum difference of the normalized MUA was larger than 0.1, the codifier was a manifestation. The codifiers of negative and positive slopes were fitted linearly and the y-intercept was subtracted from the normalized MUA to remove the baseline, as is shown in Figure 3.7 B (left column) for a particular rat. The other two codifier types were fitted by a second order polynomial and the minimum value of the normalized MUA was subtracted (Figure 3.7 B, right column, same rat). We stored all of the information about these four types of codifiers (i.e. position on the cortical sheet, type of codifier, raw LFP, and MUA data) for all experiments.

In order to confirm the difference of the spiking rate pattern between the low resolution condition and the high resolution condition, we performed two experiments to record the neuronal activities for five sound parameters (N = 2; 200 ms long; carrier frequency: 8 kHz steps, 8−40 kHz; modulator frequency: 50, 100, 200, 400 and 800 Hz; peak of amplitude: 10 dBSPL steps, 30−70 dBSPL, inter-stimulus-interval: 1.6 s, repetition: 50 trials). We classified the codifiers based on the three conditions. Eventually, we estimated the linear function for the positive and negative slope. The other two codifiers were fitted by a second order polynomial and the minimum value of the normalized MUA was subtracted.

3.7.7 Correlation analysis between spiking rate and CSD

To understand the properties of codifiers based on the PC dendritic profile of postsynaptic potentials in addition to the spiking rate, we evaluated the instantaneous correlations between the CSD amplitude/phase content at each frequency band (i.e. δ, θ, α, β, γ_L and γ_H) and the respective MUA. For evaluation of the correlations, we took into account laminar features for single trials 200 ms from the stimulus onset. To that end, we performed an ANOVA statistical analysis with multiple comparisons pooling information about the single trial correlations from all codifiers at each particular layer.

In order to illustrate the functional relationship between spiking rate and CSD, we applied a general linear model (GLM). This method was used by Whittingstall and Logothetis (2009) to investigate the PAC effect relating cortical electroencephalographic (EEG) signal and intracranial MUA. In this GLM model, the best predictors of the MUA (Y) were a linear combination of the γ_H-oscillatory amplitudes (X_1) and the δ-oscillatory phases (X_2), i.e.

$$Y = \beta_1 X_1 + \beta_2 X_2 + \varepsilon \qquad (3\text{-}1)$$

where $\beta_{1,2}$ are the coefficients of the amplitude and phase, respectively, and ε is the error term. This GLM is not useful to appropriately describe the main working hypothesis formulated by Whittingstall and Logothetis (2009) because GLM applies only to additive relationships between datasets[35]. The actual working hypothesis for the PAC is multiplicative rather than

additive, i.e. to enhance the MUA, any increase in the amplitude of the γ_H band is required to coexist with the phase-epoch of the δ band. The alternating conditional expectation (ACE) algorithm[55] provides us a proper way to test relationships between independent and dependent variables, without any a priori assumption (e.g. the GLM). An ACE regression model has the general form:

$$\theta(Y) = \alpha + \sum_{i=1}^{p} \phi_i(X_i) + \varepsilon \qquad (3\text{-}2)$$

where θ is a function of the dependent variable (response) Y, ϕ_i are functions of the independent variables (predictors) X_i ($i = 1, \cdots, p$) and ε is the error term. Therefore, the ACE regression model is robust, and could be useful to represent, not only additive models, but also multiplicative ones using logarithm functions. The particular model we are interested in testing is $Y = X_1(X_2 - \vartheta)$, which explicitly points out that MUA (Y) is maximal when the γ_H band amplitude (X_1) is also maximal and the δ oscillation (X_2) is 180^o away from the particular phase ϑ. This model can be written as an ACE regression model with the particular form:

$$Log(Y) = Log(X_1) + Log(X_2 - \vartheta) + \varepsilon \qquad (3\text{-}3)$$

Chapter 4. Results

4.1 Codification of sounds attributes

4.1.1 Spiking rate fitting corresponding to the codifiers

In Figure 4.1, we illustrated the good/bad fitting of the spiking rate based on the definition of the codifiers with high resolution stimulation conditions. First, we divided the neuronal population into four types of codifiers with a low resolution condition (e.g. f_c = 8, 24, and 40 kHz; *Amp* = 50, 200 and 800 Hz). Eventually, we obtained the goodness of fit between the estimated fitting function from three conditions and the spiking rate from five conditions (e.g. f_c = 8, 16, 24, 32 and 40 kHz; *Amp* = 50, 100, 200, 400 and 800 Hz). Most of codifiers were following the definition of codifiers with a good fitting, however, some of codifiers were not fitted well. (e.g. double peak shape, double valley shape). There are several possibilities: a) we could not record the best condition for a particular codifier with the low resolution stimulation condition; b) the sub-threshold spiking rates in the high resolution stimulation conditions were different from the low resolution stimulation conditions.

4.1.2 Codifying the sounds attributes based on the spiking rate

Some of these types of codifiers have been reported in past studies on finer analyses

of the dependency of the spike rate on the sound attributes. For example, our inverted U-shape codifier for the case of the Amp-f_c box represents roughly a kind of V-shape tuning either for frequency[86] or for sound level (Figure 1, Schreiner et al., 1992)[87]. In particular for the sound periodicity, we decided to look at neuronal populations that codify this attribute earlier based on non-temporal tuning features. In our opinion, this constitutes the first attempt to find information of sound periodicity at the very initial phase of a sound. Since we examined MUA 15 ms after the stimulus onset, there is not enough information to classify any periodic signal with a frequency of less than 66 Hz. Therefore, in our data, a modulation frequency of 50 Hz cannot be captured by any neuronal population at the time instant of 15 ms, but at this time there will be sufficient information to properly codify the 200 Hz and 800 Hz modulation frequencies.

In order to confirm whether one can satisfactorily reproduce, in terms of population, the corresponding attribute values from the spiking rate, we performed an ANOVA statistical analysis with multiple comparisons to the normalized MUA for each attribute and codifier type (Figure 4.2 **A** - f_c, **B** - f_m, **C** - *Amp*). The normalized MUA in the selected codifiers was significantly different for different attribute values. In other words, if we had already identified the codifiers in a chronic implanted rat, we could accurately determine the sound attribute value from the single trial spiking rate 15 ms after onset.

4.2 Sparse aggregation of attribute codifiers

Based on the fact that we have co-localized shanks in each experiment with respect to the main canonical vessels in the A1, we were able to differentiate the position of each codifier type (Figure 4.3). We were looking for: **a)** the presence of sparse distributions, rather than topologically-arranged dense networks, with high-heterogeneity for the selective neurons and **b)** any tendency in the organization of sound codifiers either along the tonotopic or iso-frequency axis. First, we found that positive slope codifiers for the carrier frequency f_c were mostly grouped in the most ventral part of the A1, probably in the area limiting the A1 to other sections of the primary auditory core (e.g. a fragment of the anterior auditory field, AAF) or its belt. There were three other types of codifiers distributed heterogeneously in the A1. The most abundant was the U-shape codifier, which corresponds to neurons with a tuning pattern similar to that of the L5tPC in Sakata and Harris (2009, Figure 1, sound level range: 50dB – 60 dB)[15]. Note that the size of each circle represents the density of that particular type of codifier.

In order to reproduce classic tonotopic organization, we integrated the frequency modulation f_m and amplitude Amp to calculate the mean of the spiking rate for each carrier frequency f_c. Consistent with previous studies[79),88)], we reproduced a statistically significant tonotopic organization in the A1 along the posterior-anterior axis (Figure 4.3 A, bar-plots).

However, in the section for high pure tone frequencies, it was hard to separate tones at 40 kHz from those at 24 kHz. In our opinion, this is due to the increase of Q_{10} toward the anterior section of the A1[56], which makes any tuning effect for f_c almost indistinguishable in that section of the A1. We estimated the spiking rate difference Δ between the characteristic frequency for the respective section of the A1 and the mean of the other two frequencies. The spiking rate difference is similar to the reciprocal of Q_{10}. By plotting the fraction $1/\Delta$ against the carrier frequency, we reproduced the previously reported effect that f_c has wide sensitivity in the direction of the section with the highest frequency (Figure 9 in Sally and Kelly, 1988)[56].

We found that codifiers for frequency modulation (Figure 4.3 B) and amplitude (Figure 4.3 C) were sparsely and heterogeneously distributed along the entire A1 core. Similar sparse representations have been reported in previous studies for the timbre and the sound-level (Figure 3 in Bizley et al., 2009)[12]. There was a slight tendency in the U-shape type codifier for the modulation frequency to be located at the ventral part of the A1 core. We realized that a single neuronal population could lie behind more than one codifier, which is consistent with previous studies reporting complex *Amp-f_c* mapping with tuning effects for both carrier frequency and sound level [15), 17)].

4.3 The spike-LFP relationships

4.3.1 LFP laminar profile in the frequency domain

Figure 4.4 shows the frequency characteristics of LFP in three layers. In the pre-stimulus period, LFPs were dominated by a low frequency, in particular, the power of the delta band was quite large for all layers. In the middle column, we illustrate an example of the mean Z-score spectrogram. Based on the spectrogram, we created the box plot in the right column which shows the mean Z-score for the six frequency bands in each layer. In the SG layer, we did not find a significant difference between the frequency bands. On the other hand, the Z-scores were significantly different between γ_H and the low-frequency bands (e.g. δ, θ and α) in the G and IG layers. The reason for this being that the high-frequency oscillations occurred a short period after the onset (less than 100ms). In contrast, low frequency oscillations appeared about 50 ms after the onset. Because the LFPs were stimulated by the high frequency amplitude modulated sounds, LFPs did not change frequently. The high-frequency component of the LFPs is related to the stimulus input.

4.3.2 Laminar-dependent relationships between CSD and MUA

In order to clarify the relationship between CSD and MUA, we applied a correlation analysis (Figure 4.5). The CSD-amplitude and MUA correlations in all layers were significantly different from the correlations in the non-stimulus condition (ANOVA, $p < 0.005$)

for the six frequency bands. From this result we found that, in the audio information process, high-frequency synchronizations of CSD and MUA occurred in three layers. In particular, single trial CSD (amplitude) time series for the β, γ_L, and γ_H bands were highly correlated with MUA in all layers. The correlation between CSD-amplitude content in the γ_H band and MUA was significantly larger ($p < 0.01$) in the SG layer (Figure 4.5, bottom row). In contrast, the correlation for the γ_L band was statistically larger ($p < 0.01$) in the IG layer than in the SG layer. For the β band, correlations were also significantly higher ($p < 0.01$) in the IG layer than in the other two layers. From these results, we concluded that the temporal profile of MUA underlying attribute codification is different in each layer, with relatively low (β) dynamics in the IG layer and unquestionably high dynamics (γ_H) in the SG layer. This may be related to the different laminar strategies in the A1, which have a sparse structure in the SG layers and a dense structure in the IG layers, and which underlie sound codification[15), 27)]. The correlations between the CSD-phase and MUA were less than 0.1, i.e. statistically insignificant. Indeed, we could not find any laminar structure in the relationships between the phase and MUA (data not shown).

The CSD-amplitude at the γ_H band was highly correlated to the MUA without requiring the LFP to be at the crest-phase of the low frequency bands; in particular, the δ band. Based on this result, we tested whether a phase-amplitude coupling (PAC) exists for sound

codification in anesthetized rats[35), 57), 58)]. From the ACE regression analysis applied to all single trials, using the data corresponding to all attribute codifiers, we found neither linear functions ϕ_i of the predictors nor logarithmic ones (Figure 4.6). Therefore, we concluded that sound codification in the A1 of anesthetized rats happens to occur on the basis of an interrelationship between the MUA and the CSD amplitudes for the β, γ_L, and γ_H bands and maintains no relationship to the CSD-phases of lower frequency bands.

4.4 The laminar profiles for neuron types

We determined the contributions of each type of neuron (i.e. PCs and IN) to the codification of sounds attributes as well as their respective laminar profiles. Figure 4.7 A shows the laminar distributions of the PCs and INs that were associated with all attribute codifiers evaluated at the values with the highest total spiking rates (determined from Figure 4.2 for each attribute). For all conditions, the contribution from the PCs was not only more significant than that from the INs in the SG and IG layers (as was expected), but surprisingly, it was also more significant than INs in the G layer. Sakata and Harris (2009) have provided evidence for the contribution of L4PCs in the codification of sounds[15)]. In particular, the normalized PCs-MUA of *Amp* codifiers in the SG and the IG layers were significantly larger than those for the other codifiers of PCs-MUA (f_c, f_m). The activity of putative INs was just about the same in the SG

and G layers, but in the IG layer it was a little bit higher. Furthermore, while codifying sound amplitude, the activity of INs in the IG layer decayed with respect to the other conditions. There is an interesting discussion in Sakata and Harris (2009) about the differentiated role played by these two types of neurons while processing sounds in A1[15].The contribution of each neuron type to sound attribute codification was evaluated through an ANOVA ($p < 0.01$). For all attribute codifiers (**B** – f_c, **C** – f_m, **D** – *Amp*), PCs show similar tendencies to those tendencies in Figure 4.7, which were calculated based on the MUA for all neuron types. Codification based on INs was always less significant than that obtained while using the PCs. Our results are consistent with Sakata and Harris (2009), who suggested that the sensory evoked spiking activity in the A1 is mainly based on the activity of layer 2/3 and 5 PCs[15].

Chapter 5. Discussion

In this thesis, we found that four types of sounds codifiers are distributed sparsely and heterogeneously in the A1, and PCs mainly contribute to audio information processing. In addition, the highest correlations with MUA are between the γ_H-band amplitude of CSD in the supragranular layer and the β-band amplitude of CSD in the infragranular layer. In this thesis, we proposed to establish 3D extracellular potential recording in the A1 simultaneously using MEAs for the first time. We employed a home-made silicon-based 3D probe to illustrate a topological representation of different codifiers for sound attributes based on the spiking rate of the neuronal population in the A1. Taking into account previous literature, we defined four types of codifiers, i.e. positive slope, negative slope, inverted U-shape, and U-shape; therefore our definitions may sound atypical. From our view point, such definitions captured the activity of the main codifying networks in close proximity to the electrodes. The distributions of these codifiers in the A1 were sparse and heterogeneous. To understand the input/output dynamics of these codifiers, we explored the relationships between LFP (CSD) and MUA, as well as their laminar profiles. While codifying sound attributes, the MUA in the SG and IG layers were correlated to the CSD-amplitudes of the γ_H band and the β band, respectively. The relationship

between the MUA and broad-band CSD, however, could not be described by a simple GLM. The codifications of sound attributes were mainly associated with the activity of PCs in all cortical layers. INs were also involved but to a minor degree. There was a clear distinction in the role of these two neurons for the codification of the sound levels.

5.1 Audio information processing

While listening to a symphony, our brains are not only able to discriminate whether a horn is located inside the brass section of the orchestra, but by the horn's specific timbre, they can also identify the particular moment it is played. To accomplish such tasks, the afferent segments in the auditory system of humans extracts the "what" and "where" components of the sound, which might be differentiated latterly in the respective cortical processing streams, from the audio signals. To access the spatial information in the signal, a specialized subcortical neuronal circuit processes both monaural spectra and binaural disparity alongside top-down information conveyed through the corticofugal auditory projections. This circuit involves the dorsal cochlear nucleus, the inferior colliculus and the superior olivary complex. In contrast, the codification of the major attributes of a sound, i.e. the timbre, the pitch, and the volume, have for many years now been thought to occur by means of topologically distributed assemblies of neurons exhibiting attribute-dependent tuning effects and existing at several auditory relay

regions along the whole afferent pathway.

5.2 Defining the codifiers

As we employed simple artificial pure tones whose amplitudes were modulated in time, we believe a fine exploration of attribute values is not necessary. We defined codifiers for the fundamental attributes of a sound, such as the carrier frequency (f_c), the modulation frequency (f_m), and the amplitude (*Amp*). For discrete changes in the values (three) of the attributes, we explored strategies for sound codification in the A1 and the effectiveness with which different neuronal populations achieve it. Therefore, we defined sound codifiers with the classical patterns of codifying neurons but adapted the definition to the particular case of discrete sampling. For positive and negative slope cases, the spiking rate increases or decreases with the value of the attributes. The inverted U-shape codifier is similar to that defined for the classical tuning effect while the U-shape codifier corresponds to the tuning profile of L5tPC reported by Sakata and Harris (2009, Figure 1)[15]. There are few previous studies that define such codifiers[89),105)].

In contrast, the high resolution stimulations conditions were prepared with five different parameters for each attribute of a sound. In order to observe approximately all neuronal activity in A1, we decided the stimulation conditions should have low resolution

sounds parameters instead of precise ones. Even though the low resolution stimulation condition could create complex patterns of the neuronal response map, the response of the spiking rate might include complex functions if the resolution of the stimulation condition were increased. In order to simplify neuronal population activity, one option is to not extract the response features from the extracellular recording on the mesoscopic scale; or from the point of view of engineering, to develop a brain machine interface (BMI).

In this thesis, we focused on only ON-response and found codifiers for the sound attributes. However, the neuronal responses are not only ON-set, but also OFF-set. Our stimulus condition of periodicity is more than 50 Hz; a speed at which a single neuron cannot follow the high frequency amplitude changing. On the other hand, non-synchronized neurons located in the A1 are activated during stimulation. The neurons we observed were probably of this type. If were to prepare a condition which contains low frequency amplitude modulation, we could find different types of neuronal response.

5.3 Topological sparseness

The concept of "sparseness", as defined by previous studies, originates from the fact that just a small fraction of neurons is required for sound codification, as observed in the time[76] and spatial[60] domains. In this sense, a few preferable neurons seem to be enough to properly

codify any sound attribute. Smith and Lewicki (2006) reconstructed natural complex sounds from the spikes generated by a few neurons[59]. In our study, the codifiers of sound attributes were spatially distributed and sparse in the A1 on the mesoscopic scale (Figure 4.3). Our main results regarding spatial distributions, neuronal types, and laminar profiles were consistent with those reported in previous studies, e.g. classical tonotopic organization[56), 60), 61)], the random character of the sound level representation along the A1 core[17)], the existence of a patchy organization for the neuronal activation[8)], and the particular laminar profile of several neuronal types[15)]. We did not find any evidence that the periodicity of a sound was represented either along the dorsal-ventral axis, as for cats[14)], or in a pitch-selective region close to the A1 borderline[10)], as for monkeys. However, the topological distribution of this codifier was similar to that proposed by Kilgard and Merzenich (1999)[11)] who found that pitch sensitive neurons spanned the entire A1 in rats. We partly studied the neuronal populations selective to periodicity without any distinction for pitch and modulation based stimuli. From the results of Bendor and Wang (2010), who found that modulation selective neurons were located heterogeneously in the A1 of monkeys, it seems that errors can be made if we do not properly distinguish these two properties[10)]. We did not focus our attention on neurons codifying the frequency modulation based on a temporal strategy, but on those achieving it without delay through early variations in the levels of MUA. We were able to detect the periodicity of a sound

from its first repetitive cycles, so we believe that neurons which detect periodicity of repetitive sounds with high frequencies (e.g. 800 Hz) must be crucial for rat survival and behavior.

5.4 MUA and postsynaptic activity: Dynamic relationship

In order to find the input/output relationships for the codifying neuronal population in the A1, we applied a correlation analysis between the summarized CSD and the MUA based on single trials. Several previous studies pointed out the existence of both: i) a frequency band coupling (FBC)[32), 33)] and ii) the PAC effect[35)]. Lakatos et al. (2007) examined multi-sensory interactions between the A1 and the somatosensory cortex in macaques, and later extended the analysis to investigate the interactions of auditory stimuli with the visual system, both using selective attention paradigms. They focused on the SG layer and performed a CSD analysis followed by a wavelet transform to extract the instantaneous amplitude/phase. Whittingstall and Logothesis (2009) tried to uncover the time period when high-correlations between MUA and cortical EEG signals occur in the visual cortex of monkeys[35)]. These authors employed the Hilbert transform for extracting the instantaneous amplitude/phase from EEG data. However, there was no study that explored the laminar profile of the input/output relationships underlying the codification of sound attributes. We evaluated the correlation between the CSD amplitude/phase content at each frequency-band and the respective MUA in the A1. Such a

relationship is important for understanding the role played by sub-threshold activity in the codification of sound attributes, as well as for determining the dynamic relationship of such activity with the neuronal spiking.

From our results, i.e. the correlation between CSD-amplitude (the γ_H and β bands) and MUA, we propose two hypotheses: **a)** the sound attributes have been codified along the subcortical streams and the input to the A1 already contains spatial and temporal signatures captured by our codifiers, or **b)** an incompletely processed information package reaches the A1 from the thalamus as postsynaptic activation and henceforward is used to create final sound codifiers for single attributes. Data from Sakata and Harris (2009) and Rothschild et al. (2010) support the second hypothesis[15), 27)]. These authors pointed out that sensory evoked activity propagates quickly from layer IV to layer II/III and V. They reported that small fractions in layer II/III, which are sparsely distributed, are activated in a preferable stimulus condition. From our data, we hypothesize that low (β) and high (γ_H) dynamics in the postsynaptic potentials at the respective IG (sparse) and SG (dense) layers might be associated with efficient inputs to the respective codifying neurons.

Surprisingly, we could not find either a linear or a logarithmic relationship between the CSD-content and the respective MUA, similar to what was reported by Whittingstall and Logothetis (2009) for behavior in monkeys[35)]. They, whose experiment is quite different from

ours (i.e. rats were anesthetized in an auditory evoked response paradigm[35]), recorded MUA and cortical EEG signals from the visual cortex of nonanesthetized monkeys undergoing a visual attention task. The PAC effect probably emerges only in experimental paradigms with high attentional demands in wakeful animals and is totally attenuated during the anesthesia stages. An alternative explanation is the use of different sensory-stimulus conditions. In the study by Whittingstall and Logothetis (2009), monkeys were shown to possibly process visual stimuli by combining afferent and top-down information, which may require the involvement of global neuronal networks driven by slow oscillations on the macroscale for attentional selectivity.We explored this hypothesis using quite a robust method of nonlinear/nonparametric regression, i.e. the ACE algorithm[55]. In our opinion, the mechanism for processing and codifying auditory evoked stimuli in the A1 of rats is different from that existing in the primary visual cortex of monkeys. Therefore, the relationship between LFP and the MUA could not be described by the GLM for auditory transient evoked responses.

5.5 Future perspectives

5.5.1 Physiological interpretation of EEG/MEG data

Impressive achievements on the characterization of ionic channels in principal neurons as well as on the description of their realistic morphometry has been made with the recent advances in the field of neuronal computation. The day is not far when theoretical

neuroscientists provide quantitative descriptors of the long-range visibility, as well as the particular descriptive biophysical models, of each neuronal population in the neocortex. It is fair to say that some very preliminary studies have already been performed[62) - 64)]. However, models for neurons must not be formulated based on a clamped extracellular space, as was originally proposed[65)]. Such a strong assumption constitutes a clear impediment to representing the spatial distributions of LFPs, and therefore would accentuate the gap which already exists between electrophysiologists who employ LFP and those who employ EEG data modality.

In study of EEG/LFP simultaneous recording, we have found that current monopoles constitute the most significant source component of the skull EEG in the barrel cortex of Wistar rats. Therefore, such kinds of forward/generative models must be generalized in the future to include electromotive forces that comprise quadripolar configurations for any mesoscopic region in addition to possible net outflows of monopolar origin. Furthermore, if we expand the CSD analysis from 1D to 3D, we need to consider the electrical properties of each layer, especially the conductivity profile[51)]. In this thesis, we applied the linear CSD analysis (iCSD); therefore, the conductivity in each laminar was not affected by our CSD estimation. Based on our results, we would like to suggest the following strategy to solve the EEG inverse problem in the near future:

a) Obtain characteristic dynamic equations of the multipolar current sources in the cortical

columns from biophysical models of the principal neurons. These models must be descriptive rather than exhaustive, but must take into account ionic diffusion mechanisms, as discussed above, and the relevant geometrical characteristics of neurons. However, statistical magnitudes (e.g. occurrence probability of postsynaptic currents, neuronal firing rate) impacting the states of these neuronal populations must be clearly represented.

b) Estimate the mesoscopic monopolar, dipolar and quadripolar current sources from the mesoscopic scale EEG data by solving a generalized inverse problem that makes use of both the characteristic dynamic equations and specific forward/generative models for all types of current sources. Due to the differences in EEG and MEG observation modalities, in terms of their visibility to multipolar current sources, it is recommended that this step be performed from concurrent EEG and MEG recordings.

c) Estimate the microscopic volume sources from the mesoscopic multipolar moments using equations (Appendix II, III). Finally, reconstruct the dynamics of the abovementioned statistical magnitudes from the source using the characteristic dynamic equations.

5.5.2 Application for the brain machine interface

MEAs, particularly those based on polymer aggregates and nanotechnology, are built with microelectrodes for both voltage recording and current stimulation[66], which provide excellent compatibility with brain tissues. Therefore, our strategy for codifier selection and

characterization will be helpful, not only to reconstruct the neuronal representations of sounds in the A1, but also to recreate complex sound sensations through adequate stimulation of the neural tissue in close proximity to each codifier. In other words, our method will contribute to the future development of “brain machine interfaces”, which uses a sparse electric stimulation strategy to interact with the human auditory cortex.

Chapter 6. Conclusion

In this thesis, we aimed to clarify the sound codification system of the A1 on the mesoscopic scale. To do so, we examined these main questions: **a)** the spatial aggregation to codify sound attributes in the A1; **b)** the spike-LFP relationships for codifying neuronal populations in layer II/III, IV, and V; **c)** the laminar profiles for the different neuron types of those populations that employ dissimilar schemes for attribute codification in the A1 of Wistar rats.

We established a 3D extracellular potential recording setting and developed methodology to analyze non-stationary LFPs and MUA. In order to understand the relationship between CSD and LFPS, we applied an iCSD analysis and explored the Hilbert transform to calculate the instantaneous amplitude/phase of broad frequency bands.

We found that codifiers identifying the attributes of sounds in the primary auditory cortex are distributed sparsely. In addition, the correlation between MUAs and the γ_H-band amplitude of CSD is higher in the supragranular layer. The β- and γ_L-band amplitude of CSD is highly correlated with MUA in the infragranular layer.

We concluded that, for rats, sounds are codified in A1 by a sparsely segregated

network involving specialized PCs and their postsynaptic activity may create the proper conditions for the emergence of sparse and dense spiking patterns. Furthermore, from the extracellular recording, we were able to describe, not only laminar or columnar interactions independently, but also both interactions simultaneously. To do this, we needed to consider the morphometry of the neocortex, electrical properties, and the temporal profile of neuronal activities. Our findings will be helpful to understand the genesis of the EEG signal from the multi-scale point of view. Our proposed methodologies, especially 3D extracellular recording, and findings will contribute to the analysis the huge data set recorded on the mesoscopic scale in the neocortex.

Chapter 7. Acknowledgements

First, I am greatly indebted to my supervisor, Prof. Ryuta Kawashima for the years of guidance and teaching he dedicated to my research. I treasure the time I spent in constructive discussion and brainstorming with him, and also his generous support for the installation of my experiment setting. His attitude toward science has had a great impact on me and has changed the way I view my study.

I also appreciate Prof. Jorge Riera, who supervised my Ph.D thesis from the beginning. Anytime I needed help, he patiently and kindly taught me what I needed to know. Most of the knowledge necessary to carry out this thesis, including theory, programming techniques, experimental methods, and presentation, were learned through his guidance. His ideas and suggestions opened me to a new viewpoint and drove my study.

A special thanks to Prof. Tohru Ozaki who taught me the skills for performing time series analyses, gave me his advice in many discussions, and always offered me personal support. He also contributed his considerable experience in science to making my work smooth and more coherent.

I appreciate Dr. Takakuni Goto for teaching me how to set up a laboratory and

experimental environment. Without his help, it would have been impossible to install the experimental equipment.

Additional thanks to Dr. Olivie Bertrand, Dr. Karim Jerbi, and Dr. Jérémie Mattout who collaborated with us on the relationship between LFPs and MUA. They taught me non-stationary time-frequency analysis methods and opened my mind to new methodologies.

I would like to thank Mr. Akira Sumiyoshi who motivated me enthusiastically and always discussed scientific topics with me; Ms. Sarah Michael who revised the manuscripts of my thesis, papers, and presentations, and supported me anytime I needed it. Prof. Jorge Bosch who taught me various computer skills; Prof. Pedro A Valdes Sosa who taught me statistics and data processing; and Dr. Eduald Aubert and Mr. Pedro A Valdes Fernandez who collaborated with me to create the rat-template in Havana and Sendai.

I am particularly grateful to all members of the Department of Functional Brain Imaging, especially Mr. Nonaka Hiroi who was the experiment assistant, and Ms. Yuka Konno who is the secretary of the NMD group in the Department of Functional Brain Imaging, Dr. Atsushi Sekiguchi, Dr. Rui Nouchi, Ms. Yuki Yamada, and Mrs. Haruka Nouchi who have always encouraged and motivated me. Their support along the way was essential.

Last but not least, I would like to extend my gratitude to my family, especially my parents, Toyohiro and Taeko. They have supported me through the years and continue to

encourage me to pursue and achieve my goals.

Chapter 8. References

1 Rose JR, Galambos R, Hughes JR: Microelectrode studies of the cochlear nuclei of the cat. Bull. Johns Hopkins Hosp. 104: 211-251, 1959.

2 Rose JE, Greenwood DD, Goldberg et al.: Some discharge characteristics of single neurons in the inferior colliculus of the cat. I. Tonotopical organization, relation of spike-counts to tone intensity, and firing patterns of single elements. J. Neurophysiol. 26: 294-320, 1963.

3 Tsuchitani C and Boudreau JC: Single unit analysis of cat superior olive segment with tonal stimuli. J. Neurophysiol. 29: 684-697, 1966.

4 Aitkin LM and Webster WR: Medial geniculate body of the cat: organization and responses to tonal stimuli of neurons in ventral division. J. Neurophysiol. 35: 365-380, 1972.

5 Woolsey CN and Walzl EM: Topical projection of nerve fibers from local regions of the cochlea to the cerebral cortex of the cat. Bull. Johns Hopkins Hosp. 71: 315-344, 1942.

6 Merzenich MM, Knight PL, Roth GL: Representation of cochlea within primary auditory cortex in the cat. J Neurophysiol 38: 231-249, 1975.

7 Uno H, Murai N, Fukunishi K: The tonotopic representation in the auditory cortex of the guinea pig with optical recording. Neuroscience Letters 150: 179-182, 1993.

8 Bakin JS, Kwon MC, Masino SA et al: Suprathreshold auditory cortex activation visualized by intrinsic signal optical imaging. Cereb. Cortex 6: 120-130, 1996.

9 Bendor D and Wang X: The neuronal representation of pitch in primate auditory cortex. Nature 436: 1161-1165, 2005.

10 Bendor D and Wang X: Neural coding of periodicity in marmoset auditory cortex. J Neurophysiol. 103: 1809-1822, 2010.

11 Kilgard MP, Merzenich MM: Distributed representation of spectral and temporal

information in rat primary auditory cortex. Hear. Res 134: 16-28, 1999.

12 Bizley JK, Walker KMM, Silberman B et al.,: Interdependent Encoding of Pitch, Timbre, and Spatial Location in Auditory Cortex. J. Neurosci. 29: 2064−2075, 2009.

13 Bizley JK, Walker KMM, King AJ et al.: Neural ensemble codes for stimulus periodicity in auditory cortex. J. Neurosci. 30: 5078-5091, 2010.

14 Langner G, Dinse HR, Godde B: A map of periodicity orthogonal to frequency representation in the cat auditory cortex. Front Integr Neurosci 3, 2009.

15 Sakata S, Harris KD: Laminar structure of spontaneous and sensory-evoked population activity in auditory cortex. Neuron 64: 404-418, 2009.

16 Malone BJ, Scott BH, Semple M: Temporal codes for amplitude contrast in auditory cortex. J. Neurosci. 30: 767-784, 2010.

17 Schreiner CE, Mendelson JR, Sutter ML: Functional topography of cat primary auditory cortex representation of tone intensity. Experimental Brain Research 92: 105−122, 1992.

18 Linden JF and Schreiner C: Columnar transformations in auditory cortex? A comparison to visual and somatosensory cortices. Cereb. Cortex 13: 83-89, 2003.

19 Sutter ML and Schreiner CE: Topography of intensity tuning in cat primary auditory cortex: single-neuron versus multiple-neuron recordings. J. Neurophysiol. 73: 190-204, 1995.

20 Sadagopan S and Wang X: Level invariant representation of sounds by populations of neurons in primary auditory cortex. J. Neurosci. 28: 3415-3426, 2008.

21 Watkins PV and Barbour DL: Level-tuned neurons in primary auditory cortex adapt differently to loud versus soft sounds. Cereb. Cortex 21:178−190, 2011.

22 Dantzker JL and Callaway EM: Laminar sources of synaptic input to cortical inhibitory interneurons and pyramidal neurons. Nat. Neurosci. 3: 701-707, 2000.

23 Shepherd GM and Svoboda K: Circuit analysis of experience-dependent plasticity in the developing rat barrel cortex. Neuron 38: 277-289, 2003.

24 Oviedo HV, Bureau I, Svoboda K et al.: The functional asymmetry of auditory cortex is

reflected in the organization of local cortical circuits. Nat. Neurosi. 13: 1413-1420, 2010.

25 Thomson AM and Bannister AP: Interlaminar connections in the neocortex. Cereb. Cortex 13: 5-14, 2003.

26 Smith PH and Populin LC: Fundamental differences between the thalamocortical recipient layers of the cat auditory and visual cortices. J. Comp Neurol. 436: 508-519, 2001.

27 Rothschild G, Nelken I, Mizrahi: A. Functional organization and population dynamics in the mouse primary auditory cortex. Nat Neurosci 13: 353-360, 2010.

28 Buzsáki G: Large-scale recording of neuronal ensembles. Nat. Neurosci 7: 446-451, 2004.

29 Csicsvari J, Henze DA, Jamieson B et al: Massively parallel recording of unit and local field potentials with silicon-based electrodes. J. Neurophysiol 90: 1314-1323, 2003.

30 Barthó P, Hirase H, Monconduit L et al: Characterization of neocortical principal cells and interneurons by network interactions and extracellular features. J. Neurophysiol 92: 600-608, 2004.

31 Schroeder CE, Lakatos P: Low-frequency neuronal oscillations as instruments of sensory selection. Trends Neurosci 32: 9-18, 2009.

32 Lakatos P, Chen C-M, O'Connell MN et al: Neuronal oscillations and multisensory interaction in primary auditory cortex. Neuron 53: 279-292, 2007.

33 Lakatos P, Karmos G, Mehta AD et al: Entrainment of neuronal oscillations as a mechanism of attentional selection. Science 320: 110-113, 2008.

34 Osipova D, Takashima A, Oostenveld R et al: Theta and gamma oscillations predict encoding and retrieval of declarative memory. J. Neurosci 26: 7523-7531, 2006.

35 Whittingstall K, Logothetis NK: Frequency-band coupling in surface EEG reflects spiking activity in monkey visual cortex. Neuron 64: 281-289, 2009.

36 Burns SP, Xing D, Shelley MJ et al: Searching for autocoherence in the cortical network with a time-frequency analysis of the local field potential. J. Neurosci 30: 4033-4047, 2010.

37 Martínez-Montes E, Vega-Hernández M, Sánchez-Bornot JM et al: Identifying complex brain networks using penalized regression methods. J Biol Phys 34: 315-323, 2008.

38 Ahmed B, Redissi A, Tafreshi R: An automatic sleep spindle detector based on wavelets and the teager energy operator. Conf Proc IEEE Eng Med Biol Soc 2009 : 2596-2599, 2009.

39 Contreras D, Steriade M: Spindle oscillation in cats: the role of corticothalamic feedback in a thalamically generated rhythm. J. Physiol. 490: 159-179, 1996.

40 Mitzdorf U: Current source-density method and application in cat cerebral cortex: investigation of evoked potentials and EEG phenomena. Physiol. Rev 65: 37-100, 1985.

41 Ulbert I, Heit G, Madsen J et al: Laminar analysis of human neocortical interictal spike generation and propagation: current source density and multiunit analysis in vivo. Epilepsia 45 Suppl 4: 48-56, 2004.

42 Einevoll GT, Pettersen KH, Devor A et al: Laminar population analysis: estimating firing rates and evoked synaptic activity from multielectrode recordings in rat barrel cortex. J. Neurophysiol 97: 2174-2190, 2007.

43 Pettersen KH, Devor A, Ulbert I el al: Current-source density estimation based on inversion of electrostatic forward solution: effects of finite extent of neuronal activity and conductivity discontinuities. J. Neurosci. Methods 154: 116-133, 2006.

44 Wheeler BC, Heetderks WJ: A comparison of techniques for classification of multiple neural signals. IEEE Trans Biomed Eng 29: 752-759, 1982.

45 Wood F, Fellows M, Donoghue J et al: Automatic spike sorting for neural decoding. Conf Proc IEEE Eng Med Biol Soc 6: 4009-4012, 2004.

46 Adamos DA, Kosmidis EK, Theophilidis G: Performance evaluation of PCA-based spike sorting algorithms. Comput Methods Programs Biomed 91: 232-244, 2008.

47 Takahashi S, Anzai Y, Sakurai Y: Automatic sorting for multi-neuronal activity recorded with tetrodes in the presence of overlapping spikes. J. Neurophysiol 89: 2245-2258, 2003.

48 Quiroga RQ, Nadasdy Z, Ben-Shaul Y: Unsupervised spike detection and sorting with

wavelets and superparamagnetic clustering. Neural Comput 16: 1661-1687, 2004.

49 Lewicki MS: A review of methods for spike sorting: the detection and classification of neural action potentials. Network 9: R53-78, 1998.

50 Harris KD, Henze DA, Csicsvari J et al: Accuracy of tetrode spike separation as determined by simultaneous intracellular and extracellular measurements. J. Neurophysiol 84: 401-414, 2000.

51 Goto T, Hatanaka R, Ogawa T et al: An evaluation of the conductivity profile in the somatosensory barrel cortex of Wistar rats. J Neurophysiol 104: 3388-3412 , 2010.

52 Paxinos G, Watson C: The rat brain in stereotaxic coordinates / George Paxinos, Charles Watson. Amsterdam: Elsevier, 2007.

53 Riera J, Ogawa T, Hatanaka R et al: Concurrent observations of astrocytic Ca2+ activity and multisite extracellular potentials from an intact cerebral cortex. Journal of Biophotonics 3: 147-160, 2010.

54 Li Y, Song Y, Zhao L et al: Direct labeling and visualization of blood vessels with lipophilic carbocyanine dye DiI. Nat Protoc 3: 1703-1708, 2008.

55 Wang D, Murphy M: Estimating Optimal Transformations for Multiple Regression Using the ACE Algorithm. Journal of Data Science 2: 329-346, 2004.

56 Sally SL, Kelly JB: Organization of auditory cortex in the albino rat: sound frequency. J Neurophysiol 59: 1627−1638, 1988.

57 Dalal SS, Hamamé CM, Eichenlaub JB, Karim J: Intrinsic coupling between gamma oscillations, neuronal discharges, and slow cortical oscillations during human slow-wave sleep. J. Neurosci 30: 14285−14287, 2010.

58 Le Van Quyen M, Staba R, Bragin A, Dickson C, Valderrama M, Fried I, Engel J: Large-scale microelectrode recordings of high-frequency gamma oscillations in human cortex during sleep. J. Neurosci 30: 7770−7782, 2010.

59 Smith EC, Lewicki MS: Efficient auditory coding. Nature 439: 978−982, 2006.

60 Rutkowski RG, Miasnikov AA, Weinberger NM: Characterisation of multiple physiological fields within the anatomical core of rat auditory cortex. Hear. Res. 181: 116-130, 2003.

61 Doron NN, Ledoux JE, Semple MN: Redefining the tonotopic core of rat auditory cortex: Physiological evidence for a posterior field. The Journal of Comparative Neurology 453: 345-360, 2002.

62 Gold C, Henze DA, Koch C et al: On the origin of the extracellular action potential waveform: A modeling study. J. Neurophysiol 95: 3113-3128, 2006.

63 Pettersen KH, Hagen E, Einenvall GT: Estimation of population firing rates and current source densities from laminar electrode recordings. J. Comput. Neurosci. 24: 291-313, 2008.

64 Lindén H, Pettersen KH, Einevoll GT: Intrinsic dendritic filtering gives low-pass power spectra of local field potentials. J. Compute. Neurosci. 29: 423-44, 2010.

65 Mainen ZF, Sejnowski TJ: Influence of dendritic structure on firing pattern in model neocortical neurons. Nature 382: 363-366, 1996.

66 Kipke DR, Shain W, Buzsáki G, Fetz E, Henderson JM, Hetke JF, Schalk G: Advanced neurotechnologies for chronic neural interfaces: new horizons and clinical opportunities. J. Neurosci 28: 11830-8, 2008.

Chapter 9. List of Figures

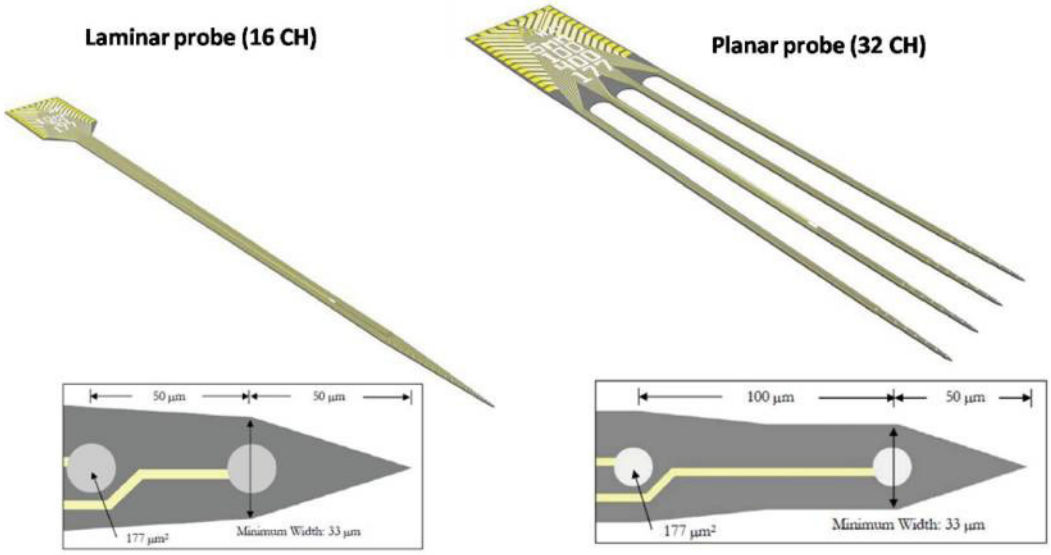

Figure 1.1 Examples of available MEAs. The laminar probe consists of 16 electrodes linearly arranged (left). The probe can be designed with variations in the distance between electrodes and the size of the electrodes. The planar probe consists of four parallel shanks, each shank having eight electrodes (right). The typical thickness of the probe is 15 µm, the typical width of the probe is 150 µm. The recording site is made of iridium, gold, and platinum metal. These probes are reusable 10–15+ times*.

---

* We received permission to publish this information from the copyright owner, NeuroNexus. The catalog of NeuroNexus can be downloaded at: http://www.neuronexustech.com/Products/ResearchProducts /MicroelectrodeArray / tabid/125/Default.aspx

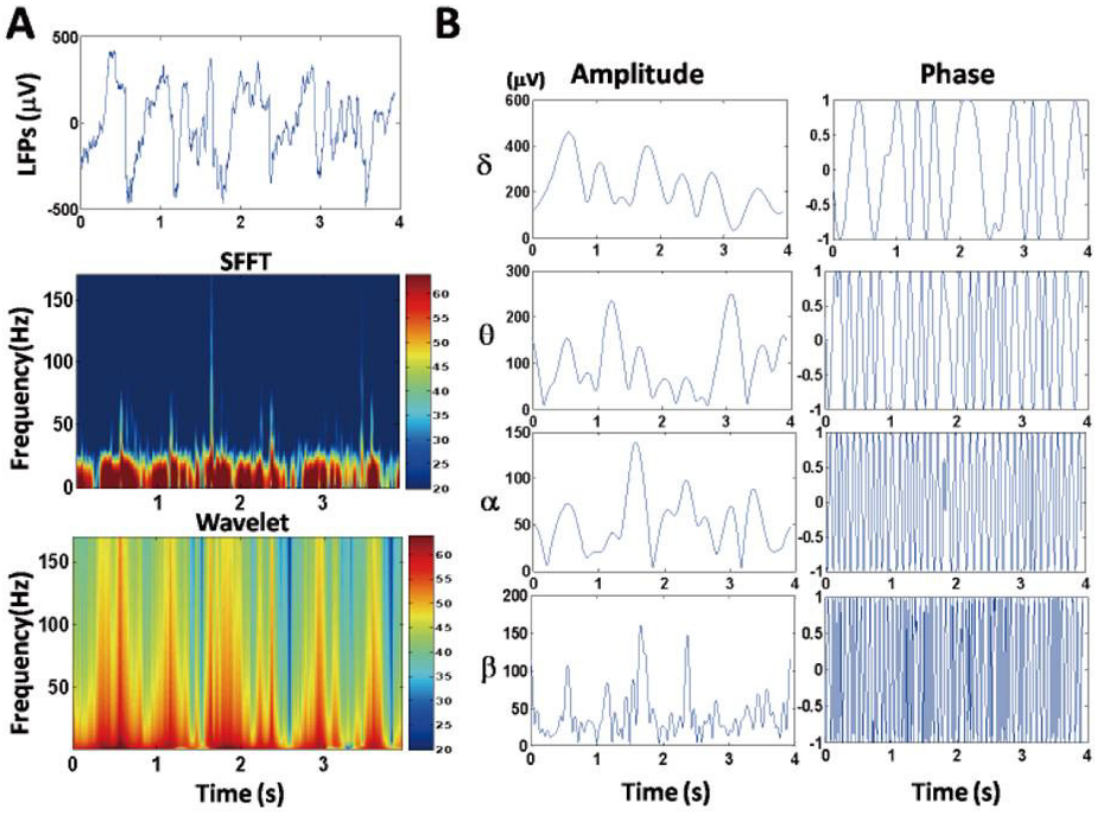

Figure 1.2 An example of the standard time-frequency analysis. (A) An example of the LFP recorded in the A1 (top) and the spectrogram of the short-time fast Fourier transform (sFFT; middle) and the wavelet transform (bottom). The duration of sample data is 4 s. The sampling frequency is 508 Hz. The colorbar shows power with the unit dB. (B) Instantaneous amplitude (left column) and phase (right column) estimated by the Hilbert transform. Before applying the Hilbert transform, LFP data was filtered through a broad frequency band (δ, θ, α, β band). The Hilbert transform calculates a particular frequency band's amplitude/phase. The LFP consists of a strong non-stationary process.

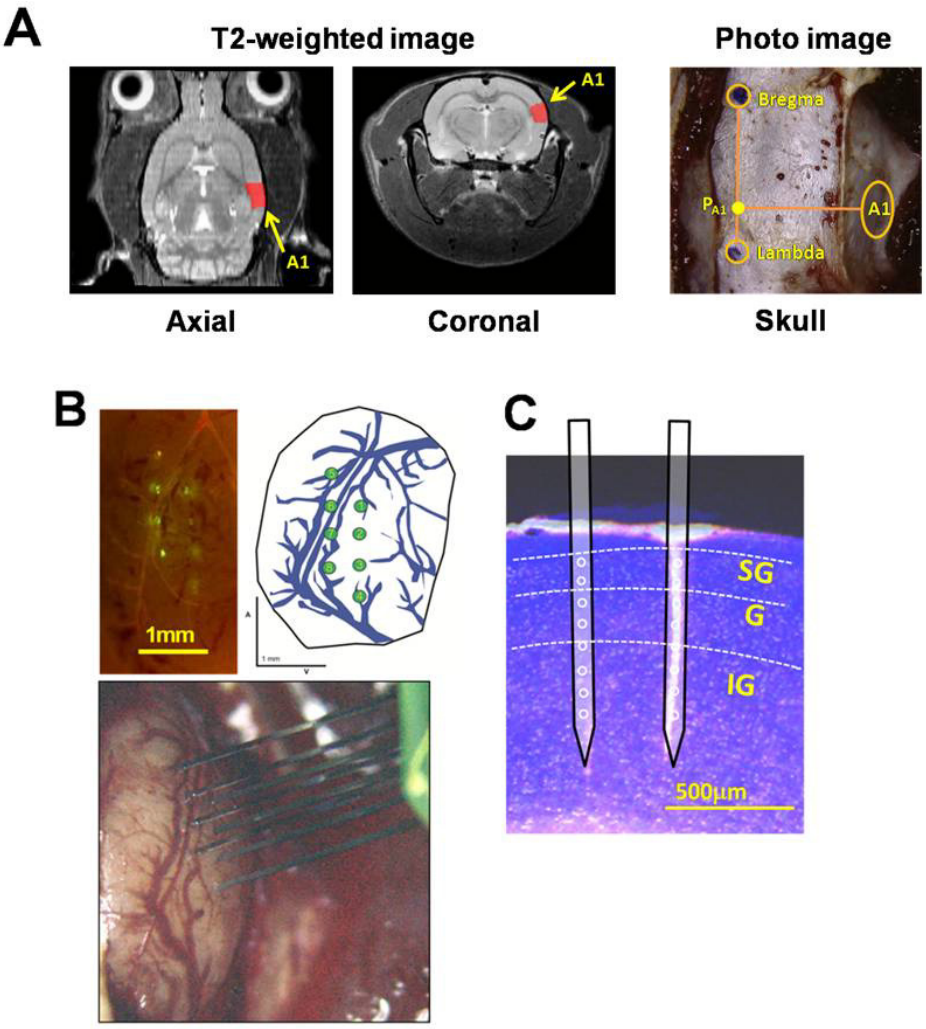

Figure 3.1 Localization of the A1 and the position of shanks and electrodes. (A) Rat brain T2-weighted images of the axial slice (left) and coronal slice (center). Based on these, we developed a strategy for stereotaxic/MRI-guidance, i.e. the bregma, the lambda and P_{A1}, and the A1 were localized accurately (right) in both the MRI (pre-surgery) and the exposed skull (surgery). (B) Co-localization of the shanks based on the vessel distribution as revealed by fluorescent staining. A fluorescent image (top left) shows the shank positions (yellow-green) and the vessel distribution (bright red) in the A1. (C) The laminar structure of the A1 and co-localization of the shanks. Depending on the Nissl stained neurons, layers were divided into three parts, supergranular (SG), granular (G), and infragranular (IG) layers.

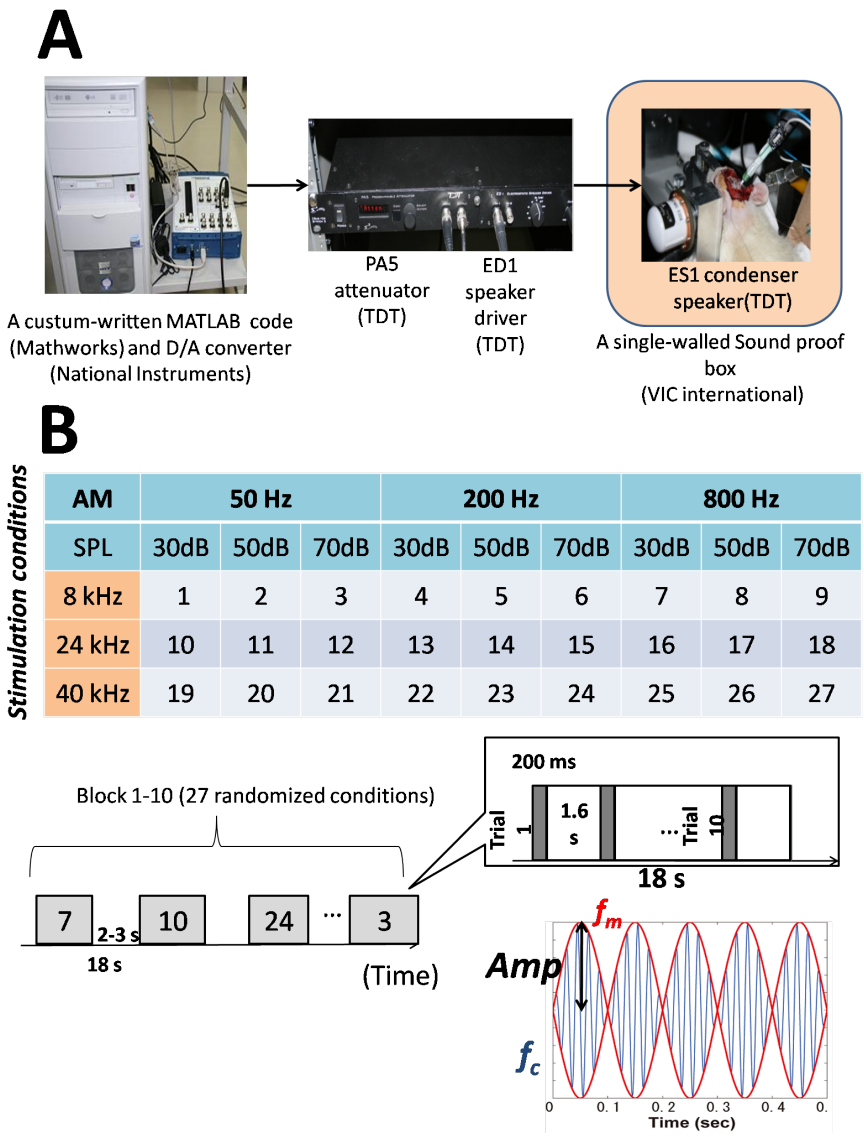

AM	50 Hz			200 Hz			800 Hz		
SPL	30dB	50dB	70dB	30dB	50dB	70dB	30dB	50dB	70dB
8 kHz	1	2	3	4	5	6	7	8	9
24 kHz	10	11	12	13	14	15	16	17	18
40 kHz	19	20	21	22	23	24	25	26	27

Figure 3.2 Auditory stimulation system and the stimulus battery of the amplitude modulation sounds. (A) The sinusoidal waveform was created by the MATLAB code. The digital signal was converted to the analog signal and conducted to the condenser speaker. (B) The amplitude modulation (AM) sounds stimulation battery. The rats were randomly stimulated by 27 prepared sounds conditions. A single condition included 10 trials (200ms; ISI: 1.6s).

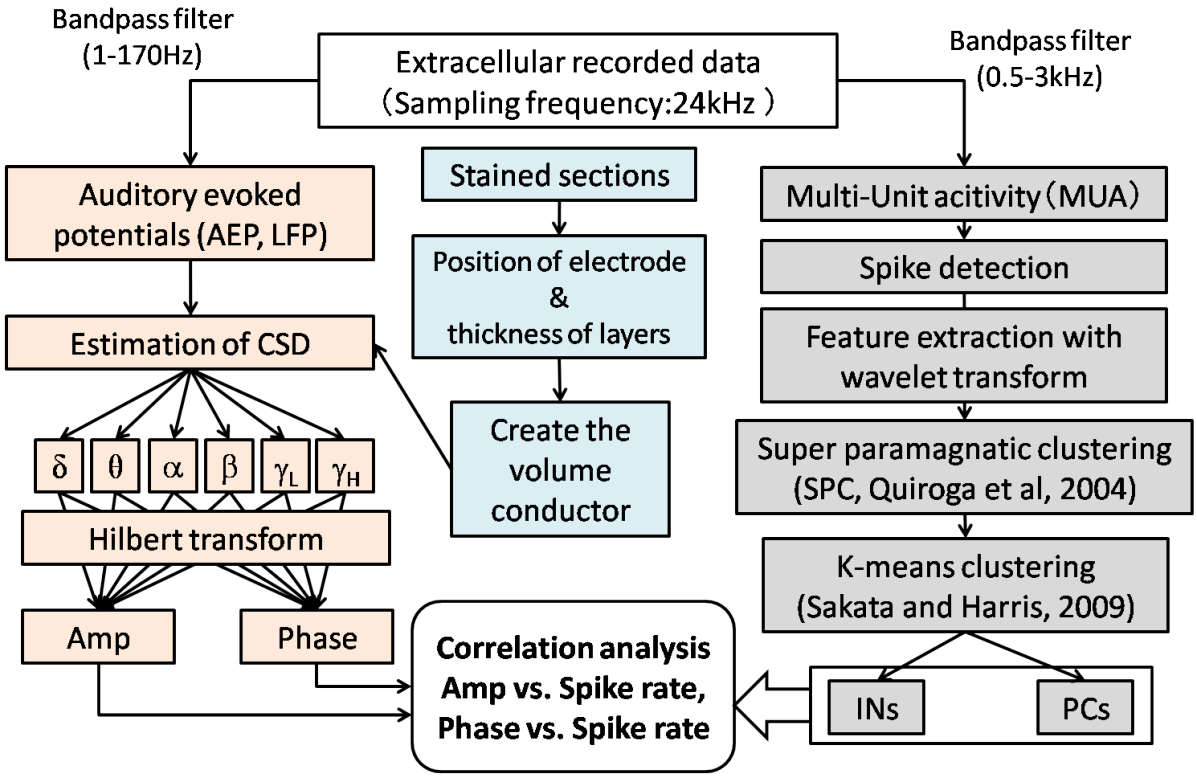

Figure 3.3 Flow chart of data analysis for extracellular recorded data. The recorded data, which was sampled at 24 kHz, was divided into two different analyses: i) a low frequency signal (LFP, left stream, beige-colored) and ii) a high frequency signal (MUA, right stream, gray-colored). In order to estimate CSD, the volume conductor model was created from the histology image (middle, blue-colored). After estimating CSD, the instantaneous amplitude/phase was decomposed to the six frequency bands. In contrast, the high frequency signal was applied to the spiking rate to classify the type of neuronal population. Accordingly, we calculated the time-series correlation between the instantaneous amplitude/phase and the spike rate.

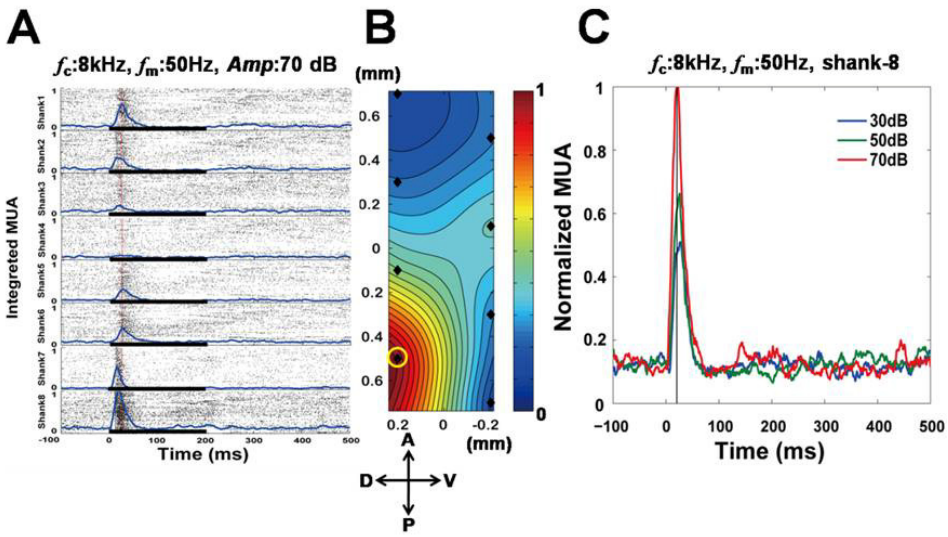

Figure 3.4 An example of the MUA analysis and identification of the single codifier (Amp). (A) The left figure shows the raster plot (black dot) and PSTH (blue line) of a 100-trial evoked response. Spikes were counted in each electrode (eight sites) on the shank. Each row corresponds to data from each shank with spikes from all electrodes overlapping. Stimulus duration was 200 ms (bold black line). The stimulus conditions in this example were: f_c = 8 kHz, f_m = 50 Hz, *Amp* = 70 dBSPL. The red line identifies the time instant of interest for attribute codification in our study, i.e. 15 ms after onset. (B) The topological mapping of the peak spiking rate at that time instant is illustrated. Black rhombi represent the positions of the shanks. A colorbar is used to represent the level of normalized MUA. (C) The peri-stimulus time histogram (PSTH) of different conditions of sound amplitudes (30dB: blue; 50dB: green; 70dB: red; the window for counting spikes: 10 ms; the moving step: 1 ms). The Y-axis represents the normalized spiking rate. These spikes were classified from data at shank-8 (yellow circle in B). Codifiers of sound attributes were identified from the normalized MUA 15 ms after the stimulus onset (black line).

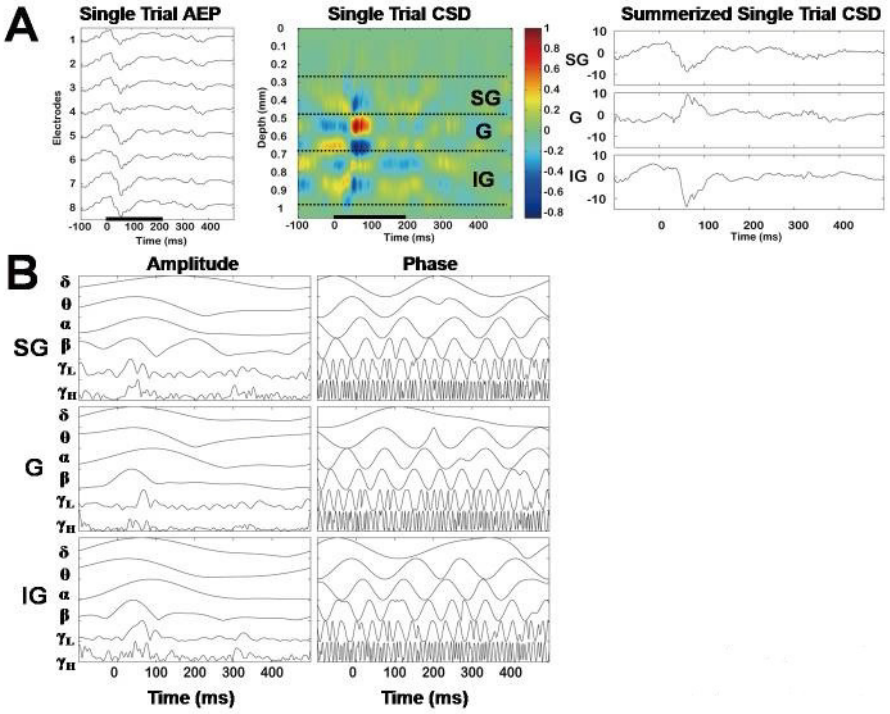

Figure 3.5 CSD analysis and decomposition of instantaneous amplitude/phase with the Hilbert transform. (A) Single trial iCSD analysis for the auditory evoked potentials (AEPs). From the single trial AEP on the same shank (left), the instantaneous CSD was estimated by the iCSD method (middle). We summarized the CSD (right) in the three layers (supragranular: SG, granular: G, and infragranular: IG). (B) An example of the instantaneous amplitude/phase in each layer obtained with the Hilbert transform. Before the transformation, bandpass filters were applied to the summarized CSDs in order to obtain the amplitude/phase content in six frequency bands (i.e. δ, θ, α, β, γL, and γH).

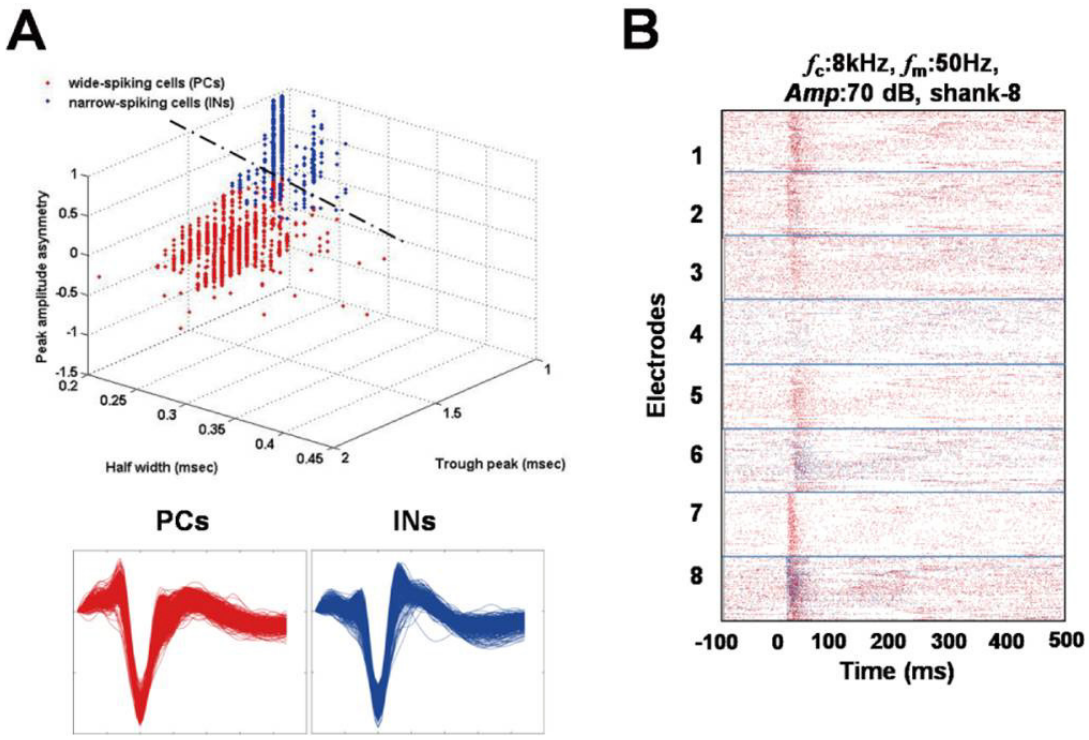

Figure 3.6 Identification of neuronal population and cell-type classification. (A) Classification of neuron types (PCs: red dot, INs: blue dot) by the SPC method[36] and K-mean clustering. In order to estimate the peak amplitude asymmetry, half width and trough peak (top), the mean waveforms of the identified neuronal populations were pooled. These three parameters were clusterized by the K-means method. The waveforms of neurons are shown in the bottom-left (PCs) and bottom-right (INs), respectively. (B) Based on the cell-classification, we were able to create separated roster plots for the PCs and INs, respectively. This figure illustrates the methodology used to create the MUA laminar profile for a particular example (i.e. f_c: 8 kHz, f_m: 50 Hz, *Amp*: 70dB).

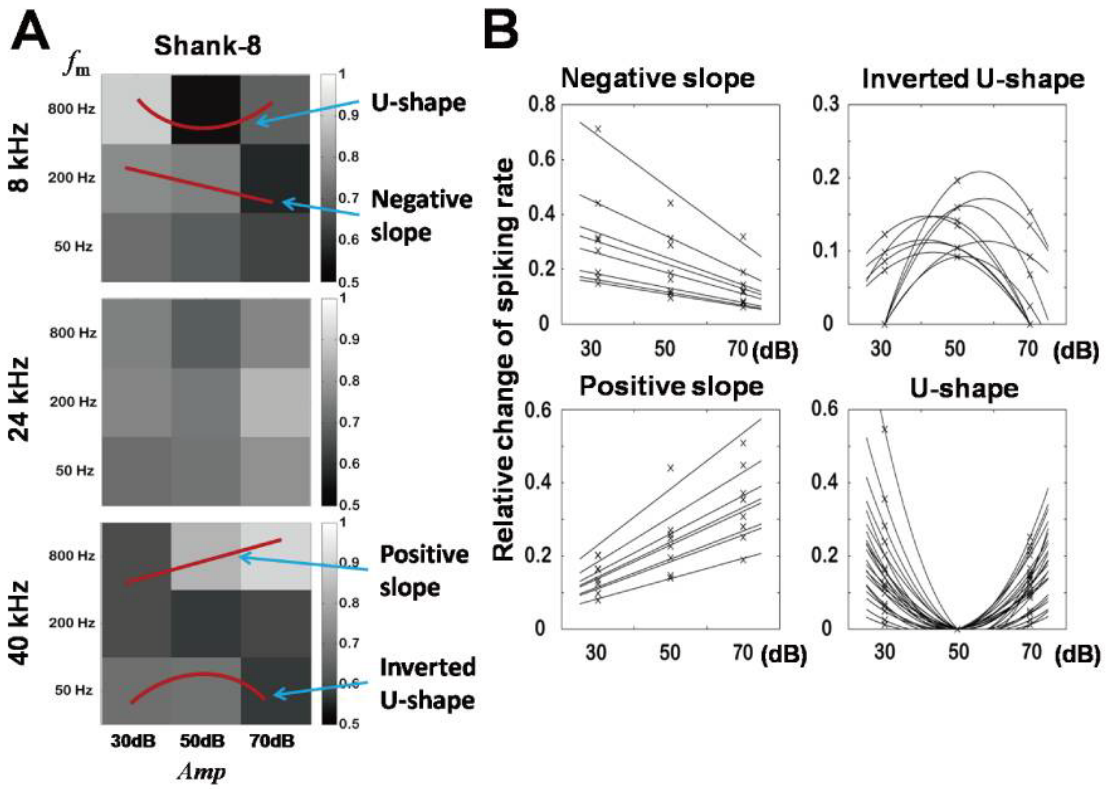

Figure 3.7 Tuning profile of population and classification of codifiers for the sound amplitude. (A) An example of the tuning profile (experiment 1, shank-8). The intensity (Amp) – frequency (f_c) response maps (gray scale) show the normalized MUA. Based on the changing tendencies of the MUA levels (in the row-direction), we classified the presence of four types of neuronal codifiers (negative slope: linearly decreasing; positive slope: linearly increasing; inverted U-shape: the maximum peak of the normalized MUA is in the middle; U-shape: the minimum peak of the normalized MUA is in middle. (B) All amplitude (*Amp*) codifiers were obtained from shanks in experiment 1. We defined these codifiers as the difference between the maximum and minimum of the normalized MUA, i.e. larger than 0.1. In the case of negative and positive slopes, we applied a linear fitting and subtracted the y-intercept to remove the baseline. For the inverted U-shape and the U-shape, we subtracted the mean of the normalized MUA of each codifier.

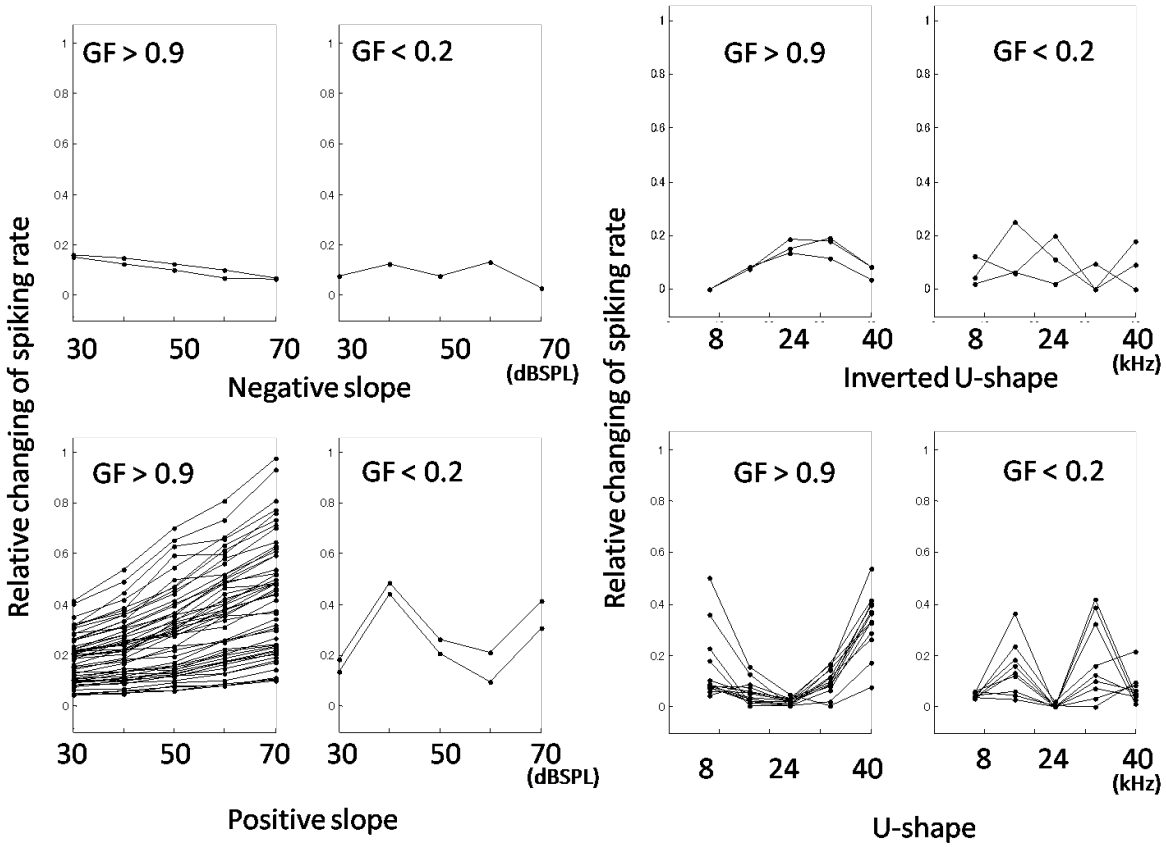

Figure 4.1 An example of the goodness of fit (GF) for each type of codifier based on the five conditions. For each codifier, the comparison of a good fitting (left, GF > 0.9) and a bad fitting (right, GF < 0.2) are shown. For the negative slope and the positive slope of the amplitude codifiers, we plotted the relative change in spiking rate. In contrast, for the inverted U-shape and the U-shape of the carrier frequency codifiers, we plotted the relative change in spiking rate. Based on the classification of three condition (30, 50, 70 dBSPL for amplitude; 8, 24, 40 kHz for the carrier frequency), most of codifiers were fitted very well to each codifier, however a part of the codifiers were not fitted.

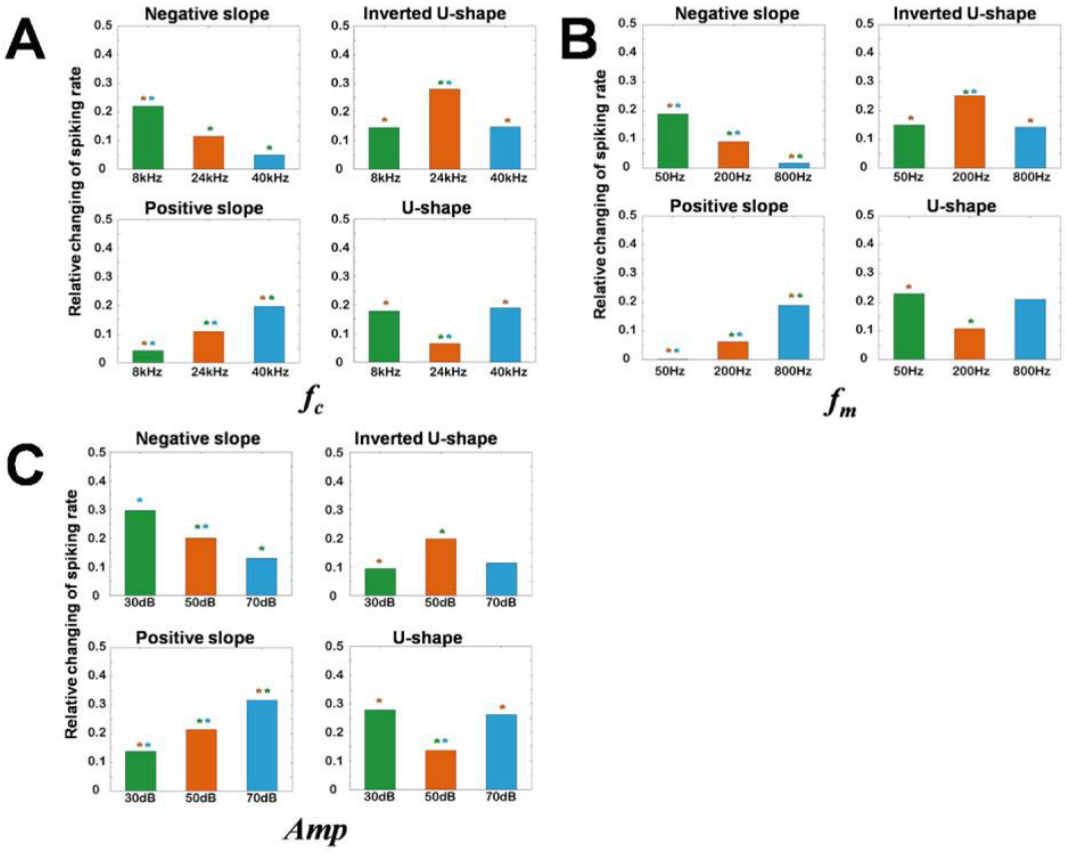

Figure 4.2 Codification of sound attributes based on the spiking rate. (A) Based on the selection of the carrier frequency (f_m), we pooled all codifiers from all experiments. The number of codifiers of each type is summarized in Table 4.6. In order to compare the different values of codifiers for a particular attribute (e.g. different carrier frequency), we employed an ANOVA with multiple comparisons. The levels of normalized MUA for the codifiers of positive and negative slopes were significantly different in each modulation frequency. (B) Same as (A), but for modulation frequency (f_m). (C) Same as (A), but for sound amplitude (*Amp*). The normalized MUA was significantly different at $p<0.01$.

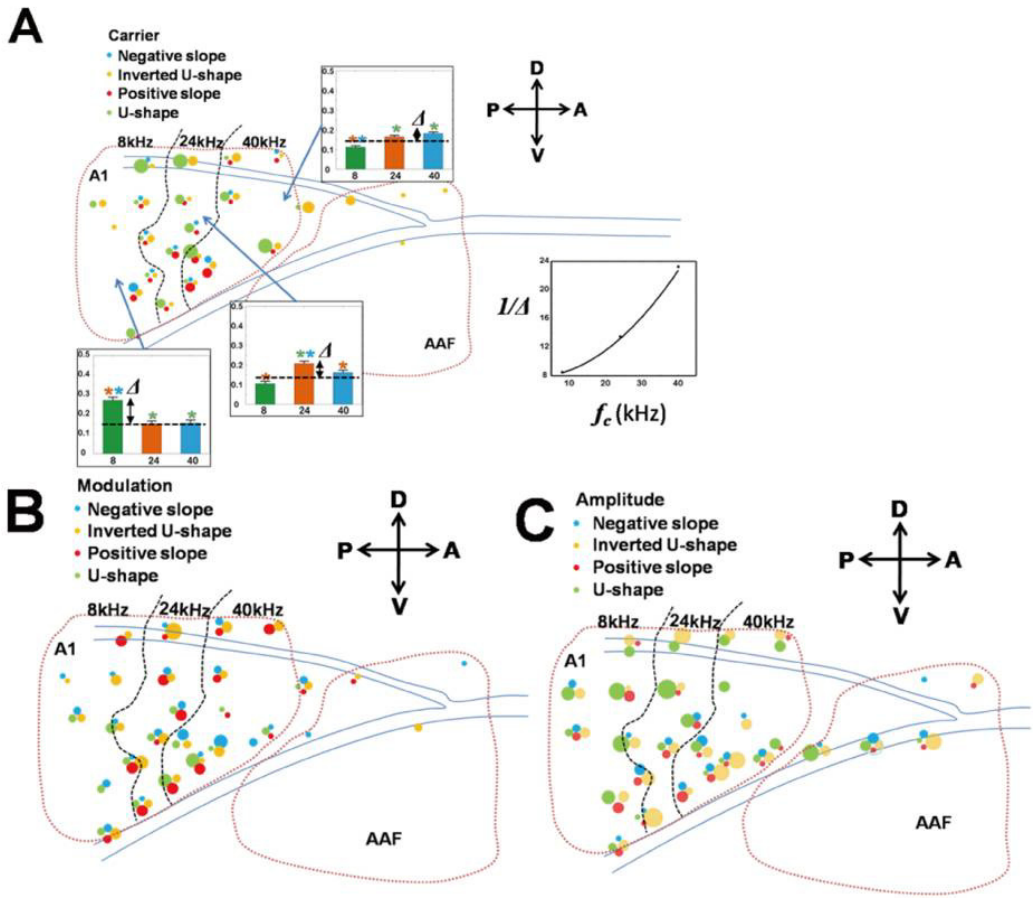

Figure 4.3 Sparse distribution of codifiers in the A1. (A) Distribution of the carrier codifiers in the A1. The integrated spiking rate shows a tonotopic distribution. The red dotted-line delimited the A1 core region and AAF; the blue line is used to represent large vessels. Colored circles show the types of codifiers (light blue: negative slope; orange: inverted U-shape; red: positive slope; green: U-shape) and the size of each circle indicates the number of codifiers at that particular site. Black dotted lines show the approximated limits for the carrier frequency based on the spiking rate in previous studies. (B), (C) Similar plots to (A), but for frequency modulation and amplitude codifiers, which were sparsely distributed in the A1.

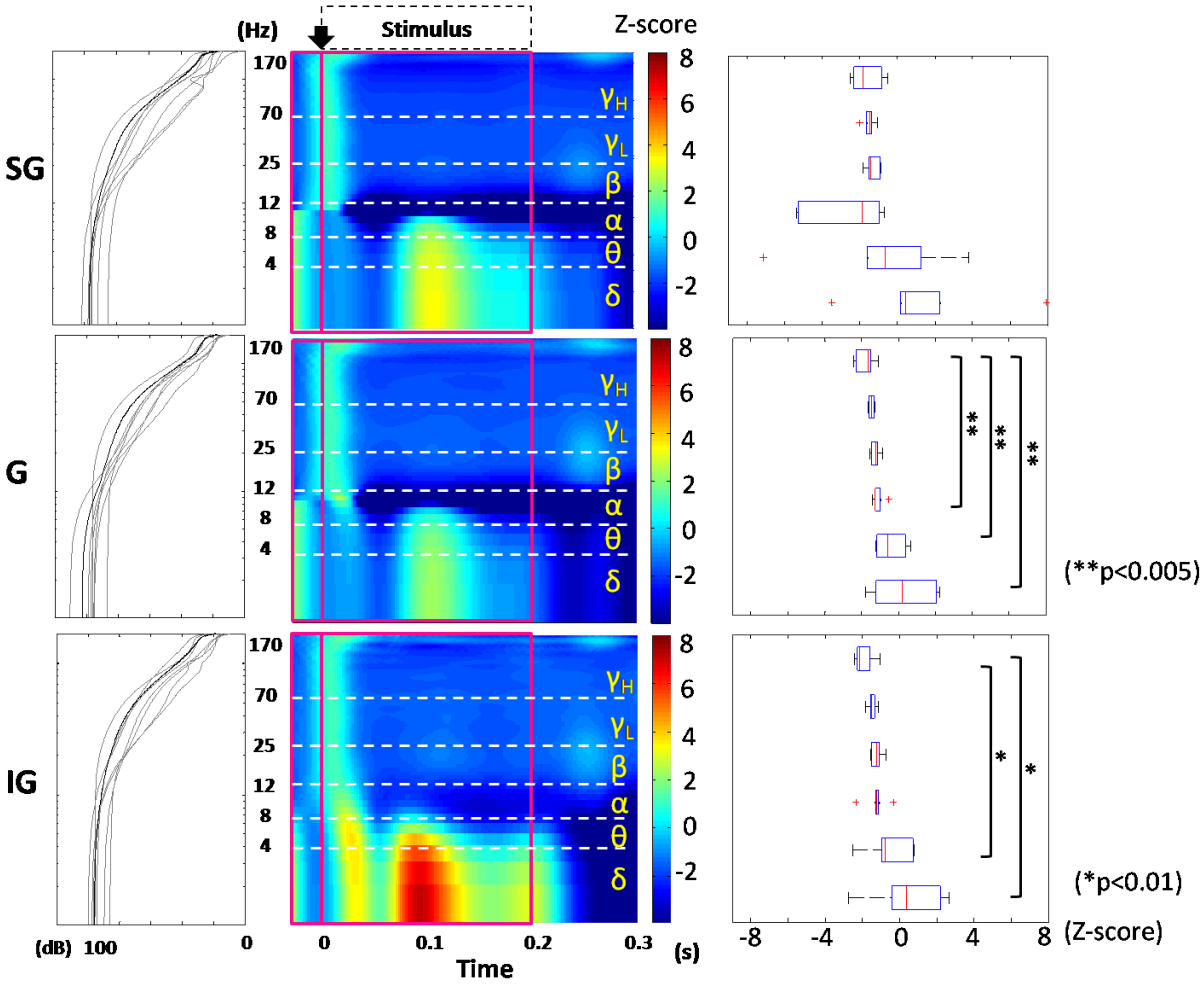

Figure 4.4 Laminar profile for LFP in the frequency domain. The three rows correspond to the three layers (SG, G and IG). The left column shows the mean power spectrum in the pre-stimulus signals (individual spectrum: gray line; the mean spectrum: black line). In order to remove the 1/f effect, we computed the Z-score by using the mean and the standard deviation in the pre-stimulus signals (left pink square). The colormaps in the middle column show the time-variant spectrum. The stimulus duration is 200 ms (right pink square), and the Y-axis was divided into six frequency bands (white dotted line). The right column shows the mean power of each frequency band within the stimulation. We evaluated those powers with ANOVA and multiple comparisons.

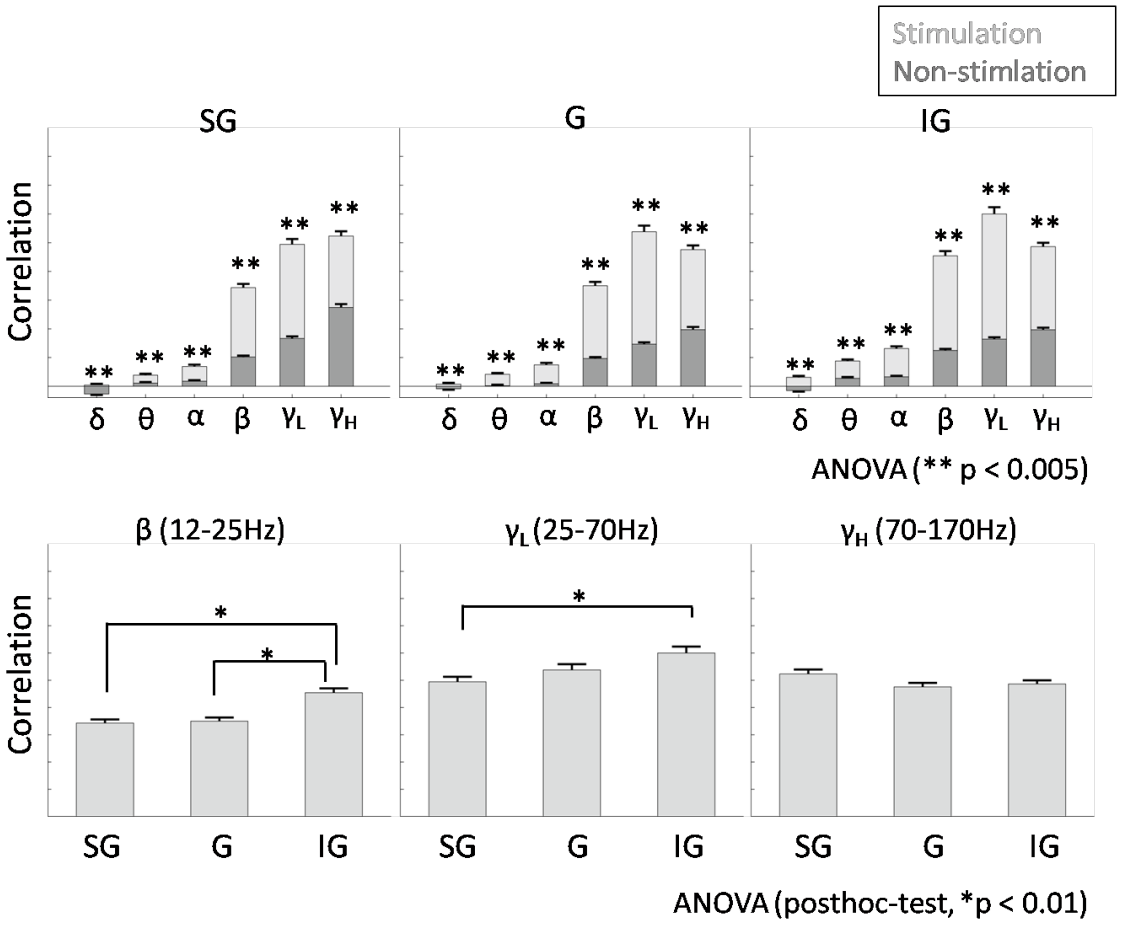

Figure 4.5 Laminar-dependency of the relationship between MUA and CSD in the frequency domain. The top row shows the correlation of a single trial MUA and instantaneous amplitude of broad band CSD, which illustrates statistical differences among frequency bands. The bright gray colored bar shows the correlation with stimulation (0-200 ms after onset). The dark colored bad shows the correlation without stimulation (300-450 ms after onset). We applied ANOVA for each frequency band ($p < 0.005$). The correlation of the β, γ_L, and γ_H bands of CSDs in all layers was high. In order to compare the correlation dependency along cortical layers, we applied the ANOVA with multiple comparisons ($p<0.01$) for the frequency bands (β, γ_L and γ_H). γ_H in the SG layer, and β and γ_L in the IG layer were highly correlated with MUA. The SG and IG layers may play important roles in the processing of sensory inputs.

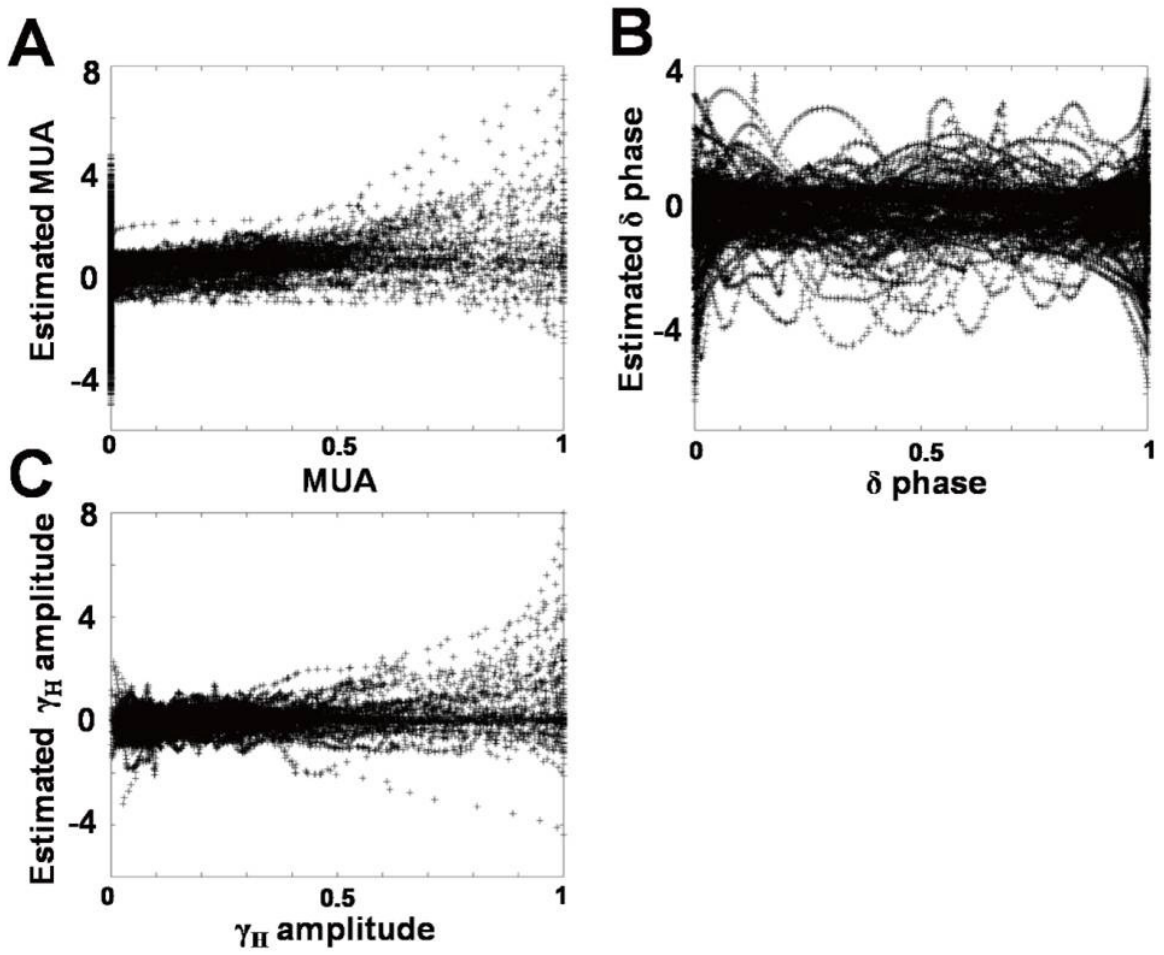

Figure 4.6 An example of the relationship between MUA, δ-phase, and γ-amplitude as modeled by the ACE method. (A)-(C): These plots show the relationships between the recorded MUA and the estimated MUA by ACE, which shows a clear nonlinear and non-logarithmic form as a function of the instantaneous δ-phase and γ-amplitude.

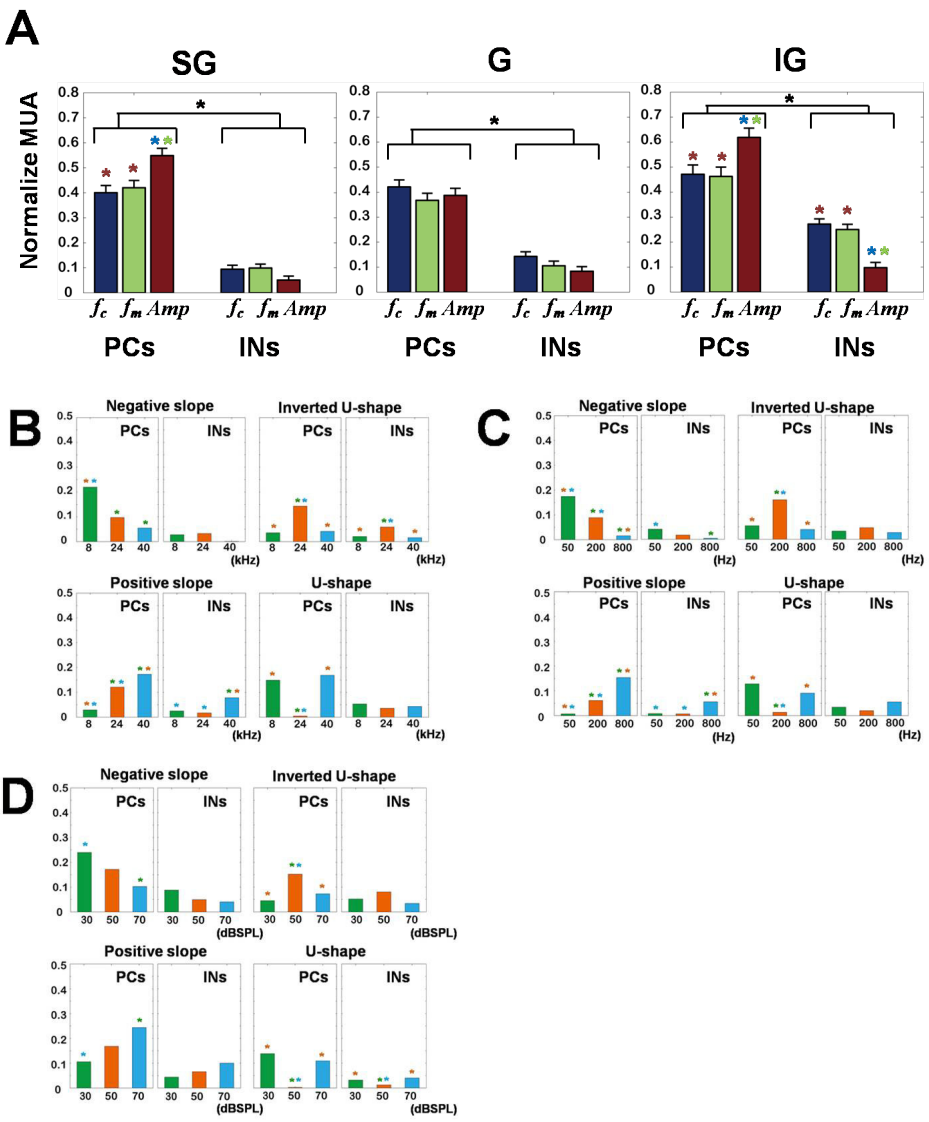

Figure 4.7 Contribution of the codifier based on neuron types. (A) Contribution of the codifier based on neuron types. We applied ANOVA to the multiple comparisons ($p<0.01$). Colored stars show a significant difference between the color bars. (B) This figure shows all e types of codifiers for the frequency carrier based on the neuron type (PCs and INs). In most cases, PCs captured the main signatures in the global MUA required to significantly codify a particular attribute of a sound. However, the contribution of INs, though smaller than that of the PCs, must not be ignored. (C) Same as (A), but for the frequency modulation. (D) Same as (A), but for the amplitude.

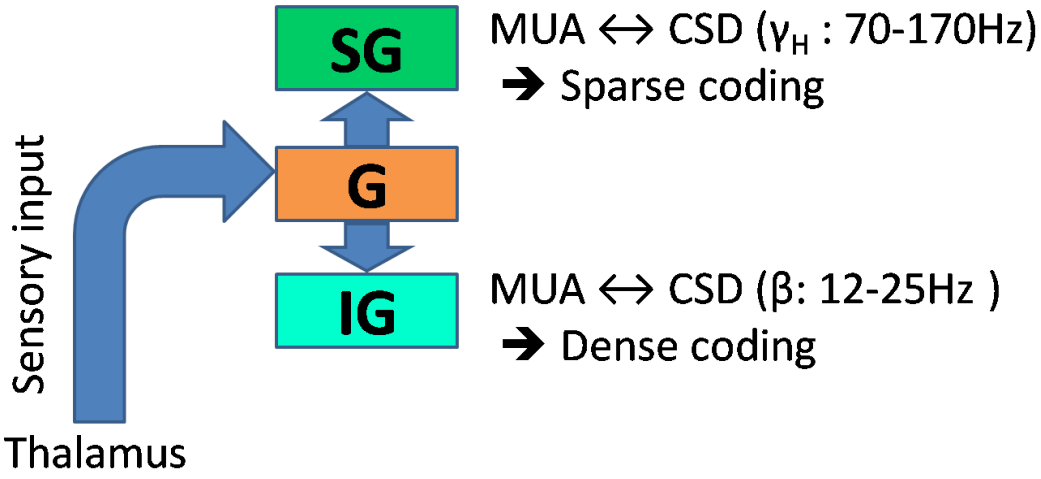

Figure 4.8 Summary of the role of auditory information processing. Sensory input move from the thalamus to the granular (G) layer, then propagates to the supragranular (SG) and the infragranular (IG) layers. In the SG layer, MUA is highly correlated to the gamma-high frequency range of CSD. In contrast, MUA is highly correlated to the beta frequency range of CSD in the IG layer.

Chapter 10. List of Tables

Table 1.1 The role of the frequency bands in LFP

Frequency band	Related phenomena
Delta (1-4 Hz)	deep sleep, anesthesia
Theta (4-8 Hz)	working memory, emotional arousal and fear conditioning,
Alpha (8-12 Hz)	convert attention, working memory & short-term memory
Beta (12-25 Hz)	top-down process, working memory & long-term memory, motor control
Gamma (30-170 Hz)	MUA, local neuronal synchronization

Table 3.1 Attributes of auditory stimulus

		V1	V2	V3
A1	Frequency (f_c)	8 kHz	24 kHz	40 kHz
A2	Amplitude (Amp)	30 dB	50 dB	70 dB
A3	Modulation (f_m)	50 Hz	200 Hz	800 Hz

A1-A3 are types of sounds attributes, V1-V3 are variables of attributes.

Table 4.6 Number of codifiers obtained from whole populations

Attribute	Negative slope	Inverted U-shape	Positive slope	U-shape
f_c	15	40	26	54
f_m	16	39	36	36
Amp	23	33	20	44

f_c: carrier frequency (8 kHz, 24 kHz, and 40 kHz); f_m: modulation frequency (50 Hz, 200 Hz, and 800 Hz); *Amp:* (30 dB, 50 dB and 70 dB).

Chapter 11. Appendix

I. The volume conductor models

The general theory

The derivation of the volume conductor models used in this paper starts with the Poisson equation described in the introduction. If we express the equation in the spherical coordinate $\vec{r} = (r, \theta, \psi)$, assuming angular symmetry and the conductivity tensor as the diagonal matrix, a detailed expression of the Poisson equation can be written as equation (I-1).

$$\frac{1}{\sigma^{\perp}} \frac{\partial}{\partial r}\left(r^2 \sigma^{\parallel} \frac{\partial \phi}{\partial r} \right) + \frac{1}{\sin\theta} \frac{\partial}{\partial \theta}\left(\sin\theta \frac{\partial \phi}{\partial \theta} \right) + \frac{1}{\sin^2\theta} \frac{\partial^2 \phi}{\partial \psi^2} = \frac{r^2 I_M}{\sigma^{\perp}} \qquad \text{(I-1)}$$

Here $\phi = \phi(\vec{r})$ are the electrical potentials, $I_M = I_M(\vec{r})$ is the CSD distribution (i.e. neuronal sources and/or sinks) defined as $I_M(\vec{r}) = \nabla \cdot \vec{J}_p(\vec{r})$, and $\sigma^{\parallel}$ and $\sigma^{\perp}$ are radial and tangential components of the diagonalized conductivity tensor $\vec{\vec{\sigma}} = diag(\sigma^{\parallel}, \sigma^{\perp}, \sigma^{\perp})$ in the spherical coordinate, respectively. For the Newman boundary condition on limiting surface S, i.e. $\partial\phi(\vec{r})/\partial n\big|_S = 0$, the integral form of equation (I-1) can be expressed as:

$$\phi(\vec{r}) = \int_{\Re} \mathbb{G}(\vec{r}, \vec{r}\,') I_M(\vec{r}\,') d\vec{r}\,'^3 + \langle \phi \rangle_S \qquad \text{(I-2)}$$

where $\mathbb{G}(\vec{r}, \vec{r}\,')$ is the Green function.

For the particular case of a monopolar current source with spherical coordinate $\vec{r}_s = (r^s, \theta^s, \psi^s)$, $I_M(\vec{r})$ can be expressed by equation (I-3).

$$I_M(\vec{r}) = \frac{I}{r^2 \sin\theta} \delta(r - r^s)\delta(\theta - \theta^s)\delta(\psi - \psi^s) \qquad \text{(I-3)}$$

where I represents the amplitude of the monopolar current source and δ is the delta Dirac function.

Infinite, homogeneous and isotropic volume conductor model

For this particular model, there is no limiting surface S. Therefore, equation I-2 can be easily integrated to yield the following result:

$$\phi\left(\vec{r}\right)=\frac{I}{4\pi\sigma\left(\left(r\right)^{2}+\left(r^{s}\right)^{2}-2rr^{s}\cos\varphi\right)^{1/2}}, \tag{I-4}$$

$$\cos\varphi=\cos\theta\cos\theta^{s}+\sin\theta\sin\theta^{s}\cos\left(\psi-\psi^{s}\right)$$

Spherical volume conductor model

For the multi-layered spherical inhomogeneous and anisotropic volume conductor model, the solution to equation (I-1) is obtained by applying the separation of variables method (de Munck, 1988):

$$\phi\left(\vec{r}\right)=\frac{I}{4\pi}\sum_{n=0}^{\infty}\left(2n+1\right)R_{n}\left(r,r^{s}\right)P_{n}(\cos\varphi), \tag{I-5}$$

where the radial Green function $R_{n}\left(\vec{r},\vec{r}^{\,s}\right)$ satisfies:

$$\frac{\partial}{\partial r}\left(r^{2}\sigma^{\|}\frac{\partial}{\partial r}R_{n}\left(r,r^{s}\right)\right)+n\left(n+1\right)\sigma^{\perp}R_{n}\left(r,r^{s}\right)=\delta(r-r^{s}) \tag{I-6}$$

The symbol P_{n} denotes the Legendre polynomials of order n.

By solving the above equation and taking into consideration the appropriate conditions of boundaries separating each layer, $R_{n}\left(r,r^{s}\right)$ can be obtained as the following series of matrix multiplications.

$$R_n(r,r^s)=$$

$$-\begin{cases}\left\{\prod_{k=K-1}^{1}M_k(r_k^d,r_{k+1}^d)M_K(r_K^d,r)\right\}_{22}\left\{M_{Ks}(r^s,r_{Ks+1}^d)\prod_{k=N_d}^{Ks+1}M_k(r_k^d,r_{k+1}^d)\right\}_{12}\Big/\{r\}^2\left\{\prod_{k=N_d}^{1}M_k(r_k^d,r_{k+1}^d)\right\}_{22}, & r^s<r\\ \left\{\prod_{k=Ks-1}^{1}M_k(r_k^d,r_{k+1}^d)M_{Ks}(r_{Ks}^d,r^s)\right\}_{22}\left\{M_K(r,r_{K+1}^d)\prod_{k=N_d}^{K+1}M_k(r_k^d,r_{k+1}^d)\right\}_{12}\Big/\{r^s\}^2\left\{\prod_{k=N_d}^{1}M_k(r_k^d,r_{k+1}^d)\right\}_{22}, & r^s>r\end{cases}$$

The suffixes attached to each brace indicate the matrix elements. The symbols K_s and K denote the number of boundaries below which a source and observation site are placed, respectively (i.e. $r_{Ks+1}^d<r^s\le r_{Ks}^d$, $r_{K+1}^d\le r<r_K^d$ for $r^s<r<r_1^d$ and $r_{Ks+1}^d\le r^s<r_{Ks}^d$, $r_{K+1}^d<r\le r_K^d$ for $r_1^d>r>r^s$).

The parameters r_k^d, with $\{k=1,\cdots,N_d\}$, represent the radii of the boundaries delimiting shells. Note that $N_d=6$ represents the number of spherical shells.

Matrices $M_k(r^a,r^b)$ are obtained by taking into account the Dirichlet and Neumann conditions at the surfaces of each layer.

$$M_k(r^a,r^b)=\begin{pmatrix}\{r^a\}^{\nu_k} & \{r^a\}^{-\nu_k-1}\\ \sigma_\parallel^k\nu_k\{r^a\}^{\nu_k-1} & -\sigma_\parallel^k(\nu_k+1)\{r^a\}^{-\nu_k-2}\end{pmatrix}\begin{pmatrix}\{r^b\}^{\nu_k} & \{r^b\}^{-\nu_k-1}\\ \sigma_\parallel^k\nu_k\{r^b\}^{\nu_k-1} & -\sigma_\parallel^k(\nu_k+1)\{r^b\}^{-\nu_k-2}\end{pmatrix}^{-1},$$

$$\nu_k=\frac{1}{2}\left(-1+\sqrt{1+4n(n+1)\frac{\sigma_\perp^k}{\sigma_\parallel^k}}\right)$$

It is known that equation (I-5) converges poorly for $r\approx r^s$ and requires a high computational cost to calculate. Therefore, some method to reduce the computation time is necessary. To satisfy this requirement, we apply a combination of the asymptotic approximation and the addition-subtraction method (de Munck and Peters, 1993; de Munck, 1994) to equation (I-5). First, we apply the asymptotic expansion to ν_k and get the following first order approximation function of $R_n(r,r^s)$:

$$(2n+1)R_n(r,r^s)=-A\Lambda^n\left(F+\mathrm{O}\left(n^{-1}\right)\right), \qquad \text{(I-7)}$$

$$A=\begin{cases}\prod_{j=K}^{Ks-1}\lambda_j^{1/(2\alpha_j-1)}\dfrac{\lambda_s^{1/(2\alpha_{Ks}-1)}}{\lambda^{1/(2\alpha_K-1)}}, & r^s<r\\ \prod_{j=Ks}^{K-1}\lambda_j^{1/(2\alpha_j-1)}\dfrac{\lambda^{1/(2\alpha_K-1)}}{\lambda_s^{1/(2\alpha_{Ks}-1)}}, & r^s>r\end{cases},\ \Lambda=\begin{cases}\prod_{j=K}^{Ks-1}\lambda_j^{\alpha_j}\dfrac{\lambda_s^{\alpha_{Ks}}}{\lambda^{\alpha_K}}, & r^s<r\\ \prod_{j=Ks}^{K-1}\lambda_j^{\alpha_j}\dfrac{\lambda^{\alpha_K}}{\lambda_s^{\alpha_{Ks}}}, & r^s>r\end{cases},$$

$$F=\begin{cases}\dfrac{1}{r\beta_{Ks}}\prod_{Ks-1}^{j=K}\dfrac{2\beta_{j+1}}{\beta_j+\beta_{j+1}}, & r^s<r\\ \dfrac{1}{r^s\beta_K}\prod_{K-1}^{j=Ks}\dfrac{2\beta_{j+1}}{\beta_j+\beta_{j+1}}, & r^s>r\end{cases},$$

where,

$\lambda=\dfrac{r}{r^K}$, $\lambda_s=\dfrac{r^s}{r^{Ks}}$, $\lambda_j=\dfrac{r^{j+1}}{r^j}$, $\alpha_j=\sqrt{\sigma_j^{\parallel}/\sigma_j^{\perp}}$, and $\beta_j=\sqrt{\sigma_j^{\parallel}\sigma_j^{\perp}}$.

By the addition-subtraction method with equation (I-7), the final form of equation (I-5) can be obtained:

$$\phi(\vec{r})=\frac{I}{4\pi}\left\{\sum_{n=0}^{\infty}\left[(2n+1)R_n(r,r^s)+AF\Lambda^n\right]P_n(\cos\varphi)-AF\left(\frac{1}{\sqrt{1-2\Lambda\cos\varphi-\Lambda^2}}-1\right)\right\} \tag{I-8}$$

Note that $R_n(r,r_s)$ is the actual radial Green function and not the approximated one (I-7).

A unified formalism

For computational reasons, we would like to represent the solution to equation I-2 for the three volume conductor models used in this study as a unified form. Note that in practice the electric potentials are observed in a discrete number of electrodes with spherical coordinates $\vec{r}_e=(r^e,\theta^e,\psi^e)$. Equation I-2 can be written as a function of a generalized Green function:

$$\phi(\vec{r}_e)=G(\vec{r}_e,\vec{r}_s;\Theta)I \tag{I-9}$$

With the following **particular cases**:

A - For the infinite, homogeneous and isotropic (*InfH*) volume conductor model

$$G_{inf}\left(\vec{r}_e,\vec{r}_s;\Theta\right)=\frac{1}{4\pi\sigma\left(\left(r\right)^2+\left(r^s\right)^2-2rr^s\cos\varphi\right)^{1/2}}, \qquad \text{(I-10a)}$$

$\Theta=\{\sigma\}$, with σ as the conductivity of the medium.

B - For the spherical volume conductor models

$$G_{sph}\left(\vec{r}_e,\vec{r}_s;\Theta\right)=\frac{1}{4\pi}\sum_{n=0}^{\infty}\left[\left(2n+1\right)R_n\left(r^e,r^s\right)+AF\Lambda^n\right]P_n\left(\cos\varphi_e\right) - \frac{AF}{4\pi}\left(\frac{1}{\sqrt{1-2\Lambda\cos\varphi_e-\Lambda^2}}-1\right) \qquad \text{(I-10b)}$$

$$\cos\varphi_e=\cos\theta^e\cos\theta^s+\sin\theta^e\sin\theta^s\cos\left(\psi^e-\psi^s\right)$$

- $\Theta=\{\mathbf{R}_D,\sigma\}$ for the spherical homogeneous and isotropic (*SphH*) volume conductor model, where $\mathbf{R}_D=\{r^d\}$ comprises only the radius of the limiting sphere and σ represents the conductivity of the sphere.
- $\Theta=\{\mathbf{R}_D,\boldsymbol{\sigma}\}$ for the spherical inhomogeneous and anisotropic (*SphIh*) volume conductor model, where $\mathbf{R}_D=\{r_k^d;k=1,\cdots,N_d\}$ comprises the radii of all boundaries delimiting shells (Table 4.3) and the conductivity profile $\boldsymbol{\sigma}=\{\sigma_{\parallel}^k,\sigma_{\perp}^k\}$ comprises the radial and tangential conductivity values for all shells.

II. The nonlinear optimization method

For the estimation of the conductivity profile, we employed the spherical inhomogeneous and anisotropic volume conductor model (*SphIh*). In a spherical conductive medium, a potential observed by an electrode positioned at position $\vec{r}_e$, responding to a

monopolar current source $I_i(t)$ at position $\vec{r}_s^{\,i}$, can be represented by equation (I-9) $\phi^i(\vec{r}_e,t) = G_{sph}(\vec{r}_e,\vec{r}_s^{\,i};\Theta) I_i(t)$, with the generalized Green function defined by equation (I-10b).

Therefore, the voltage difference between a recording electrode $\vec{r}_r^{\,e}$ and a common reference $\vec{r}_{REF}$ is defined by:

$$\hat{V}_e^i(t) = \phi^i(\vec{r}_e,t) - \phi^i(\vec{r}_{REF},t) \tag{II-1}$$

$$\hat{V}_e^i(t) = \left(G_{sph}(\vec{r}_e,\vec{r}_s^{\,i};\Theta) - G_{sph}(\vec{r}_{REF},\vec{r}_s^{\,i};\Theta)\right) I_i(t)$$

The parameter set $\Theta = \{\mathbf{R}_D, \boldsymbol{\sigma}\}$ contains information about the conductivity profile. The radii of all boundaries delimiting shells (i.e. the cortical layers) are obtained from immunostaining methods. Therefore, by applying the Fourier transform, we can define the voltage differences as a function of the injected current for each frequency component through the linear function $f_{e,i}(\boldsymbol{\sigma}) = G_{sph}(\vec{r}_e,\vec{r}_s^{\,i};\Theta) - G_{sph}(\vec{r}_{REF},\vec{r}_s^{\,i};\Theta)$, which therefore depends on

$$\hat{V}_e^i(\omega) = f_{e,i}(\boldsymbol{\sigma}) I_i(\omega) \tag{II-2}$$

The optimization problem can be represented as a large nonlinear regression model with respect to the unknown parameter $\boldsymbol{\sigma}$ (II-3) by constructing the voltage differences and current injections vectors $\hat{V} = \left(\hat{V}_1^1, \hat{V}_2^1, \cdots, \hat{V}_{N_e}^1, \cdots \hat{V}_1^{N_i}, \cdots, \hat{V}_{N_e}^{N_i}\right)'$ and $I = \left(I_1, I_2, \cdots, I_{N_i}\right)'$, respectively. Note that $\hat{V}_e^i = \hat{V}_e^i(\omega_c)$ and $I_i = I_i(\omega_c)$ represent the values of these magnitudes at the particular frequency $\omega_c = 500Hz$ of the sinusoidal injection current.

$$\hat{V} = F(\boldsymbol{\sigma}) I \tag{II-3}$$

$$F(\boldsymbol{\sigma}) = \begin{pmatrix} f_{1,1}(\boldsymbol{\sigma}) & \cdots & f_{1,N_i}(\boldsymbol{\sigma}) \\ \vdots & \ddots & \vdots \\ f_{N_e,1}(\boldsymbol{\sigma}) & \cdots & f_{N_e,N_i}(\boldsymbol{\sigma}) \end{pmatrix}$$

This matrix is created for the position of the microelectrodes in the planar MEA (N_e recording sites) and the laminar MEA (N_i injecting sites).

In the same way, we defined the large vector of actual data as $V=\left(V_1^1,V_2^1,\cdots,V_{N_e}^1,\cdots V_1^{N_i},\cdots,V_{N_e}^{N_i}\right)'$. The final nonlinear least square optimization problem can be defined by equation (II-4).

$$\boldsymbol{\sigma}=\arg\min_{\boldsymbol{\sigma}}\left\|V-F\left(\boldsymbol{\sigma}\right)I\right\|^2 \qquad \text{(II-4)}$$

We applied the trust region method (Coleman and Li, 1994, 1996; *lsqcurvefit* MATLAB function) to solve II-4.

III. LORETA solution

We modeled the continuous neuronal density of source/sink $I_M\left(\vec{r}\right)$ as a set of N_d discrete electric current monopoles $I_M\left(\vec{r}\right)=\sum_{m=1}^{N_m}I_m\delta\left(\vec{r}-\vec{r}_m\right)$ defined on a high-resolution volumetric grid which covers the whole region of interest with positions $\vec{r}_m\in\mathbf{R}_M$. The new inverse problem then consisted of estimating the monopole value I_m in all lattices of the grid from a column vector $\mathrm{V}=\left(V_1,V_2,\cdots,V_{N_e}\right)'$ comprising the LFP observed at each time instant from $N_e=128$ microelectrodes regularly distributed inside $\Re$.

Under such a discretization approach for monopoles and microelectrodes, equation (I-1b) transforms into an algebraic equation system (II-1), which can be solved independently for each time instant.

$$\mathrm{V}=\mathbf{G}\mathrm{M}+\eta \qquad \text{(III-1)}$$

We assumed the presence of uncorrelated normally distributed instrumental noise $\eta \sim N\left(0,\upsilon^2 I\right)$. The discrete generalized Green function matrix $\mathbf{G}=\left\{G\left(\vec{r}_e,\vec{r}_m;\Theta\right)\right\}$ was calculated by evaluating the theoretical expression for a layered anisotropic spherical volume conductor (Eq. 10, de Munck et al., 1989) in the microelectrode $\vec{r}_e$ and monopole $\vec{r}_m$ positions, additionally using the statistics of the conductivity profile obtained in this work for the barrel cortex.

The column vector $\mathrm{M}=\left(I_1,I_2,\cdots,I_{N_m}\right)'$ comprises the monopole values. Typically, the number of electric current monopoles is larger than the number of microelectrodes $N_m >> N_e$. Also, in principle, the kernel $G\left(\vec{r}_e,\vec{r}_m;\Theta\right)$ has a non-trivial null space. Hence the matrix $\mathbf{G}$ is not a full rank and is in very bad conditioned. The use of a priori information about $I_M\left(\vec{r}\right)$ has become a standard way to deal with this problem, giving rise to the well known "*distributed inverse solution*" family. Low resolution electrical tomography (LORETA), which results from the application of a vector Laplacian penalty functional to the PCD, constitutes one of the most acknowledged distributed inverse solutions (Pascual-Marqui, 1994) so far. LORETA can be interpreted within the context of the *general smoothing splines* introduced by Wahba (1990) to solve noisy operator equations (Riera et al., 2006). LORETA inverse solution will, not only guarantee smoothness of the reconstructed $I_M\left(\vec{r}\right)$, but it will also force the $I_M\left(\vec{r}\right)$ to be minimal on the boundary of the brain.

Technically, the LORETA-type inverse solution for equation (III-1) results from minimizing the optimization function $o\left(\mathrm{M}\right)=\left\|\mathrm{V}-\mathbf{G}\mathrm{M}\right\|^2+\lambda^2\left\|\mathbf{L}\mathrm{M}\right\|^2$ with respect to the monopole value vector M. The solution of such a weighted linear regression problem is:

$$\hat{\mathrm{M}}=\left(\mathbf{G}'\mathbf{G}+\lambda^2\mathbf{L}'\mathbf{L}\right)^{-1}\mathbf{G}'\mathrm{V} \qquad \text{(III-2)}$$

The estimation of the hyperparameters λ is a problem of considerable importance since it tells us about the accuracy of the electrophysiological instrument as well as the degree of smoothness to be introduced for $I_M(\vec{r})$. In this paper, we used the generalized cross validation (GCV) method to estimate λ (Wahba, 1990).

$$\hat{\lambda}^2 = \frac{\|\mathrm{PV}\|^2}{\left[\mathrm{tr}(\mathrm{P})\right]^2} \quad \text{Projecting matrix: } \mathrm{P} = \mathrm{I} - \mathbf{G}\left(\mathbf{G}'\mathbf{G} + \lambda^2\mathbf{L}'\mathbf{L}\right)^{-1}\mathbf{G}' \qquad \text{(III-3)}$$